Supplementary Material (1) to accompany ***Investigating the Influence of Diffusional Coupling on Mixture Permeation across Porous Membranes***

Experimental Membrane Permeation Data; Comparisons with Maxwell-Stefan Simulations with Simulation Data Inputs

Rajamani Krishna* and Jasper M. van Baten

Van 't Hoff Institute for Molecular Sciences, University of Amsterdam, Science Park 904,

1098 XH Amsterdam, The Netherlands

*CORRESPONDING AUTHOR Tel +31 20 6270990; Fax: + 31 20 5255604;

email: r.krishna@uva.nl

Table of Contents

1. Abstract

Explicit analytic expressions for the permeation fluxes of binary mixtures across porous membranes are derived.

2. Introduction

In this first of two Supplementary Materials to accompany our article *Investigating the Influence of Diffusional Coupling on Mixture Permeation across Porous Membranes*, we derive analytic expressions for the permeation fluxes across porous membranes using the Maxwell-Stefan diffusion formulation.

The Figures accompanying this Appendix A contain the experimental membrane permeation data, along with inputs (pure component isotherm fits, Maxwell-Stefan data on diffusivities $Đ_1$, $Đ_2$, and $Đ_{12}$ used in the simulations to match the binary mixture permeation experiments.

3. Maxwell-Stefan equations for mixture diffusion

The Maxwell-Stefan (M-S) equations for *n*-component diffusion inside porous crystalline materials can be written as

$$-\phi \frac{c_i}{RT}\nabla\mu_i = \sum_{\substack{j=1\\ j\neq i}}^{n} \frac{x_j N_i - x_i N_j}{Đ_{ij}} + \frac{N_i}{Đ_i}; \quad i = 1,2,...n \tag{1}$$

In equation (1) the $Đ_i$ is the M-S diffusivities of species *i*, portraying the interaction between component *i* in the mixture with the surface, or wall of the structure. The fluxes N_i defined in equation (1) are expressed in terms of the number of moles of species *i* transported per m^2 of *crystalline material* per second. The $Đ_{ij}$ are M-S exchange coefficients representing interaction between component *i* with component *j*. The c_i are the loadings, defined in terms of moles per m^3 of *accessible* pore volume, within the pore.

The pore concentrations c_i are related to the molar loadings q_i by the expression

$$c_i = \frac{\rho q_i}{\phi} = \frac{q_i}{V_p} \tag{2}$$

where ρ represents the framework density, ϕ represents the fractional pore volume, and V_p is the m^3 accessible pore volume per kg of framework. It is to be noted that the ϕ appears in the M-S equations (1) because the c_i are defined in terms of pore volume and not the total volume of the crystals. The c_i are useful measures when comparing different materials. We will have occasion to use both c_i and the molar loadings q_i.

An equivalent formulation of the M-S equations uses the molar loadings q_i as concentration measures

$$-\rho \frac{q_i}{RT} \nabla \mu_i = \sum_{\substack{j=1 \\ j \neq i}}^{n} \frac{x_j N_i - x_i N_j}{Đ_{ij}} + \frac{N_i}{Đ_i}; \quad i = 1,2,..n \tag{3}$$

in which the M-S diffusivities, $Đ_i$ and $Đ_{ij}$, have the same significance, and magnitudes as in equations (1).

The x_i in equations (1) and (3) represent the component mole fractions in the adsorbed phase within the pores

$$x_i = q_i / q_t = \quad c_i / c_t; \quad 1,2,.....n \tag{4}$$

where q_t and c_t are the *total* mixture loadings and pore concentrations, respectively:

$$q_t = \sum_{i=1}^{n} q_i; \quad c_t = \sum_{i=1}^{n} c_i;$$

The Onsager reciprocal relations require

$$Đ_{ij} = Đ_{ji} \tag{5}$$

By defining an n-dimensional square matrix $[B]$ with elements

$$B_{ii} = \frac{1}{Đ_i} + \sum_{\substack{j=1 \\ j \neq i}}^{n} \frac{x_j}{Đ_{ij}}; \qquad B_{ij} = -\frac{x_i}{Đ_{ij}}; \quad i, j = 1,2....n \tag{6}$$

We can recast eq. (1) into the following form

$$-\phi\frac{c_i}{RT}\nabla\mu_i=-\rho\frac{q_i}{RT}\nabla\mu_i=\sum_{j=1}^{n}B_{ij}N_j;\quad i=1,2,..n \tag{7}$$

The chemical potential gradients $\nabla\mu_i$ can be related to the gradients in the pore concentrations, $c_{i,}$ and the gradients of the molar loadings, q_i, by defining thermodynamic correction factors Γ_{ij}

$$\frac{q_i}{RT}\nabla\mu_i=\sum_{j=1}^{n}\Gamma_{ij}\nabla q_j;\quad \frac{c_i}{RT}\nabla\mu_i=\sum_{j=1}^{n}\Gamma_{ij}\nabla c_j;\quad \Gamma_{ij}=\frac{q_i}{p_i}\frac{\partial p_i}{\partial q_j}=\frac{c_i}{p_i}\frac{\partial p_i}{\partial c_j};\quad i,j=1,....n \tag{8}$$

In the general case, the elements of the matrix of thermodynamic correction factors Γ_{ij} must be determined by numerical differentiation of the equations describing adsorption equilibrium. For description of adsorption equilibrium, the Ideal Adsorbed Solution Theory (IAST) of Myers and Prausnitz [1] is of sufficient accuracy and is used consistently in this work.

Equation (7) can be re-written in *n*-dimensional matrix notation as

$$-\phi\ [\Gamma]\nabla(c)=-\rho\ [\Gamma]\nabla(q)=[B](N) \tag{9}$$

In proceeding further with our development we denote the inverse of [*B*] as [Δ]:

$$[B]^{-1}\equiv[\Delta] \tag{10}$$

For the special case of a binary mixture, *n* =2, the four elements of the matrix [*B*] are given explicitly as follows

$$B_{11}=\frac{1}{Đ_1}+\frac{x_2}{Đ_{12}} \tag{11}$$

$$B_{22}=\frac{1}{Đ_2}+\frac{x_1}{Đ_{12}} \tag{12}$$

$$B_{12}=-\frac{x_1}{Đ_{12}} \tag{13}$$

$$B_{21}=-\frac{x_2}{Đ_{12}} \tag{14}$$

The elements of the matrix [Δ] can be derived from the inverse of [B]

$$[\Delta] \equiv [B]^{-1} = \begin{bmatrix} \frac{1}{Đ_1} + \frac{x_2}{Đ_{12}} & -\frac{x_1}{Đ_{12}} \\ -\frac{x_2}{Đ_{12}} & \frac{1}{Đ_2} + \frac{x_1}{Đ_{12}} \end{bmatrix}^{-1} \tag{15}$$

The matrix inversion can be carried out explicitly to give the following expressions

$$\Delta_{11} = Đ_1 \frac{\left(1 + \frac{x_1 Đ_2}{Đ_{12}}\right)}{1 + \frac{x_1 Đ_2}{Đ_{12}} + \frac{x_2 Đ_1}{Đ_{12}}} \tag{16}$$

$$\Delta_{22} = Đ_2 \frac{\left(1 + \frac{x_2 Đ_1}{Đ_{12}}\right)}{1 + \frac{x_1 Đ_2}{Đ_{12}} + \frac{x_2 Đ_1}{Đ_{12}}} \tag{17}$$

$$\Delta_{12} = Đ_1 \frac{\frac{x_1 Đ_2}{Đ_{12}}}{1 + \frac{x_1 Đ_2}{Đ_{12}} + \frac{x_2 Đ_1}{Đ_{12}}} \tag{18}$$

$$\Delta_{21} = Đ_2 \frac{\frac{x_2 Đ_1}{Đ_{12}}}{1 + \frac{x_1 Đ_2}{Đ_{12}} + \frac{x_2 Đ_1}{Đ_{12}}} = \frac{x_2}{x_1} \Delta_{12} \tag{19}$$

In the limiting case of $x_1 \to 1; \quad x_2 \to 0$ we obtain

$$\Delta_{11} = \frac{Đ_1 \left(1 + \frac{x_1 Đ_2}{Đ_{12}}\right)}{1 + \frac{x_1 Đ_2 + x_2 Đ_1}{Đ_{12}}} \to Đ_1; \quad x_1 \to 1; \quad x_2 \to 0 \tag{20}$$

In the limiting case of $x_2 \to 1; \quad x_1 \to 0$ we obtain

$$\Delta_{22} = \frac{Đ_2\left(1+\frac{x_2 Đ_1}{Đ_{12}}\right)}{1+\frac{x_2 Đ_1 + x_1 Đ_2}{Đ_{12}}} \to Đ_2; \quad x_2 \to 1; \quad x_1 \to 0 \tag{21}$$

4. Analytic expressions for the thermodynamic correction factors Γ_{ij}

It is useful to develop simple analytic expressions for the thermodynamic correction factors. Analytic expressions for Γ_{ij} can be derived for the case in which the component loadings follow the mixed-gas Langmuir isotherm

$$\theta_i = \frac{q_i}{q_{i,sat}} = \frac{c_i}{c_{i,sat}} = \frac{b_i p_i}{1+\sum_{i=1}^{n} b_i p_i}; \quad i = 1,2,...n \tag{22}$$

Carrying out the differentiation in eq. (8) the elements of [Γ] are

$$\Gamma_{ij} = \frac{q_{i,sat}}{q_{j,sat}}\left(\delta_{ij} + \frac{\theta_i}{\theta_V}\right); \quad i, j = 1,..n \tag{23}$$

where δ_{ij} is the Kronecker delta. The fractional vacancy θ_V is defined by:

$$\theta_V = \left(1-\theta_1-\theta_2-....-\theta_n\right) \tag{24}$$

The mixed-gas Langmuir model (22) is thermodynamically inconsistent, except when the saturation adsorption capacities of all component species are equal [2]; in this case, the elements of [Γ] for binary mixtures further simplifies to yield

$$[\Gamma] = \frac{1}{1-\theta_1-\theta_2}\begin{bmatrix} 1-\theta_2 & \theta_1 \\ \theta_2 & 1-\theta_1 \end{bmatrix} \tag{25}$$

5. Unary permeation fluxes and permeances

For pure component adsorption, the thermodynamic correction factor is

$$\Gamma_i = \frac{1}{1-\theta_i} \tag{26}$$

For the special case of unary diffusion of component *i* equation (3) simplifies to

$$N_i = -\rho Đ_i \Gamma_i \frac{dq_i}{dz} \tag{27}$$

The Maxwell-Stefan diffusivity, $Đ_i$ is generally a function of the occupancy or loading. For a given guest molecule, the loading dependence is influenced by a variety of factors including pore size, pore topology and connectivity [3-6]. For structures in which correlation effects are particular strong, such as MFI, MgMOF-74, NiMOF-74, FAU, the M-S diffusivities, $Đ_i$, often show a linear dependence on the number of vacant positions available, i.e.

$$Đ_i(\theta) = Đ_i\ \theta_V \tag{28}$$

For this scenario, combining equation (26), (27), and (28) yields

$$N_i = -\rho Đ_i \frac{dq_i}{dz} \tag{29}$$

The absence of the thermodynamic correction factor is remarkable; this is a result of the fact that the "correction" for the loading dependence of the M-S diffusivities cancels out with the "thermodynamic correction factor". We will see below that such cancellation effects also manifest for mixture diffusion.

This simple expression (29) can be integrated across a porous crystalline layer of thickness δ to obtain the following expression for the steady-state unary permeation fluxes

$$N_i = \frac{\rho Đ_i}{\delta} \Delta q_i \tag{30}$$

The unary permeance, Π_i^0, is obtained by dividing by the trans-membrane pressure difference

$$\Pi_i^0 \equiv \frac{N_i}{\Delta p_i} \tag{31}$$

In this work equations (30), and (31) are used to back out the values of the membrane transport coefficients $\frac{\rho Đ_1}{\delta}$, and $\frac{\rho Đ_2}{\delta}$ from experimental data on unary permeation fluxes and permeances. These values of $\frac{\rho Đ_1}{\delta}$, and $\frac{\rho Đ_2}{\delta}$ are then used for estimation of the permeances for binary mixtures, with additional assumptions regarding the values of the degrees of correlation.

6. Maxwell-Stefan modeling of binary mixture permeation

We now derive the appropriate set of equations to describe binary mixture permeation at *steady state* across a porous crystalline layer of thickness δ. In our theoretical development, the resistance of the support layer is ignored. Furthermore, the micro-porous crystalline layer is considered to be defect-free, and inter-grain boundary resistances have been ignored.

At steady-state, the molar fluxes N_i obey

$$\frac{\partial N_i}{\partial z} = 0 \tag{32}$$

The steady state permeation fluxes N_i are obtained determined by solving the set of two coupled differential equations (9), subject to the boundary conditions

$$\begin{aligned} &z = 0; \quad p_i = p_{i0}; \quad c_i = c_{i0}; \quad q_i = q_{i0} \\ &z = \delta; \quad p_i = p_{i\delta}; \quad c_i = c_{i\delta}; \quad q_i = q_{i\delta} \end{aligned} \tag{33}$$

It is convenient to define the driving forces for trans-membrane transport

$$\Delta q_i = q_{i0} - q_{i\delta}; \quad \Delta c_i = c_{i0} - c_{i\delta}; \quad i = 1,2 \tag{34}$$

In our earlier works we have solved the set of equations (9), (33) and (34) using rigorous numerical porcedures that takes account of the loading dependence of the M-S diffusivities, $Đ_1$, and $Đ_2$ [7-9].

Exact *analytic* solutions to the set of equations (9), (33) and (34) are possible when equation (28) for the loading dependence is invoked, along with the expression (25) for the thermodynamic correction factors [10]. The obtained expressions, corresponding to equation (44) of Krishna and Baur [10] are

$$N_1 = \frac{\rho Đ_1}{\delta}\left[\frac{\left(1+\frac{x_1 Đ_2}{Đ_{12}}\right)\Delta q_1 + \frac{x_1 Đ_2}{Đ_{12}}\Delta q_2}{1+\frac{x_1 Đ_2}{Đ_{12}}+\frac{x_2 Đ_1}{Đ_{12}}}\right] \tag{35}$$

and

$$N_2 = \frac{\rho Đ_2}{\delta}\left[\frac{\frac{x_2 Đ_1}{Đ_{12}}\Delta q_1 + \left(1+\frac{x_2 Đ_1}{Đ_{12}}\right)\Delta q_2}{1+\frac{x_1 Đ_2}{Đ_{12}}+\frac{x_2 Đ_1}{Đ_{12}}}\right] \tag{36}$$

The remarkable feature of the exact analytic solution is that the "correction" factor for the loading dependence of the M-S diffusivities, effectively cancels out the "thermodynamic correction factor". Indeed this "canceling out" effect is precisely analogous to that witnessed for unary permeation in equation (30). The accuracy of these simple results presented in equations (35), and (36) have been established by detailed comparisons with numerical solutions in our earlier work [10]. While such cancelling out effects are the *combined result* of two *special* scenarios, described by equations (25) and (28). The final obtained equations are of more general applicability and not restricted to these chosen special scenarios; this have been verified by comparing with rigorous numerical solutions [11, 12] of the equations taking all factors into consideration.

Another important point to note is that though the derivation of the equations (35), and (36) uses the mixed gas Langmuir isotherm to obtain simplified analytic solutions, the pore loadings in equations (35), and (36) are determined with the rigorous IAST calculations of thermodynamic equilibrium in all cases considered in our paper.

Strictly speaking equations (35), and (36) are "exact" only for the case where the saturation capacities of the constituent species are identical; it provides a good approximation when the saturation capacities are different.

The component permeances in the binary mixture can be obtained from

$$\Pi_i \equiv \frac{N_i}{\Delta p_i}; \quad i = 1,2 \tag{37}$$

In the general case, for each component, the permeance determined from equation (37) is different from that determined from unary permeation experiments. These differences are largely traceable to the degrees of correlation. The permeation selectivity is defined as

$$S_{perm} = \frac{\Pi_1}{\Pi_2} = \frac{N_1/\Delta p_1}{N_2/\Delta p_2} \tag{38}$$

It is convenient to define the adsorption selectivity, S_{ads}, in terms of the component loadings and partial pressures in the upstream compartment.

$$S_{ads} = \frac{q_{10}/q_{20}}{p_{10}/p_{20}} \tag{39}$$

In further discussions it is useful to define the diffusion selectivity of the membrane, S_{diff}:

$$S_{diff} = \frac{S_{perm}}{S_{ads}} \tag{40}$$

If the downstream partial pressures $p_{1\delta}$, and $p_{2\delta}$, and component loadings $q_{1\delta}$, and $q_{2\delta}$ are negligible in comparison with the corresponding upstream values, the following expression S_{diff} can be derived using equations (35), and (36)

$$S_{diff} = \frac{Đ_1}{Đ_2}\left[\frac{\left(1+\frac{x_1 Đ_2}{Đ_{12}}\right)q_{10} + \frac{x_1 Đ_2}{Đ_{12}} q_{20}}{\frac{x_2 Đ_1}{Đ_{12}} q_{10} + \left(1+\frac{x_2 Đ_1}{Đ_{12}}\right)q_{20}}\right]\frac{q_{20}}{q_{10}} = \frac{Đ_1}{Đ_2}\left[\frac{\left(1+\frac{x_1 Đ_2}{Đ_{12}}\right)x_1 + \frac{x_1 Đ_2}{Đ_{12}} x_2}{\frac{x_2 Đ_1}{Đ_{12}} x_1 + \left(1+\frac{x_2 Đ_1}{Đ_{12}}\right)x_2}\right]\frac{x_2}{x_1} \tag{41}$$

which simplifies to yield

$$S_{dfff} = \frac{Đ_1}{Đ_2}\left[\frac{\left(1+\frac{x_1 Đ_2}{Đ_{12}}\right)x_1 + \frac{x_1 Đ_2}{Đ_{12}}x_2}{\frac{x_2 Đ_1}{Đ_{12}}x_1 + \left(1+\frac{x_2 Đ_1}{Đ_{12}}\right)x_2}\right]\frac{x_2}{x_1} = \frac{Đ_1}{Đ_2}\frac{\left(1+\frac{Đ_2}{Đ_{12}}\right)}{\left(1+\frac{Đ_1}{Đ_{12}}\right)} \quad (42)$$

where we have invoked the relation

$$x_1 + x_2 = 1 \quad (43)$$

A good approximation to equation (42) is

$$S_{diff} \approx \frac{D_{1,self}}{D_{2,self}} \quad (44)$$

which is the ratio of self-diffusivities in the *mixture*. The detailed proof of equation (44) is available in the Supplementary Material accompanying our previous publication. Self-diffusivities are significantly to determine from MD simulations, and equation (44) serves as an adequate measure of diffusion selectivities in mixture diffusion.

7. Methodology adopted for interpretation of mixture permeation experiments

For interpretation of the experimental data on binary mixture permeation the following step-wise procedure is followed.

(1) The first step is to estimate the membrane transport coefficients $\frac{\rho Đ_1}{\delta}$, and $\frac{\rho Đ_2}{\delta}$ ffrom experimental data on unary permeation fluxes and permeances using equations (30), and (31). For these calculations the pure component molar loadings obtained from dual-Langmuir Freundlich fits of pure component isotherms in most cases. For SAPO-34 membranes, the fits are using the Statistical isotherm [13]. The fit parameters used for this purpose are specified in the attached Figures accompanying this Supporting Material.

(2) The estimated values of the membrane transport coefficients $\frac{\rho Đ_1}{\delta}$, and $\frac{\rho Đ_2}{\delta}$ are used for calculation of the steady-state fluxes N_1 and N_2 for binary mixtures for a range of upstream pressures using equations (35) and (36). In these calculations, the component loadings at the upstream face q_i of the membrane are calculated using the Ideal Adsorbed Solution Theory (IAST) of Myers and Prausnitz [1]. The pure component isotherm fits are the same as those used in step (1) above. For the estimation of the steady-state fluxes and permeances, additional information is required on the *degrees of correlations*, $\frac{Đ_1}{Đ_{12}}$, and $\frac{Đ_2}{Đ_{12}}$. There is only one adjustable parameter in view of the fact that the ratio $\frac{Đ_1}{Đ_2}$ is simply the ratio of the membrane transport coefficients. In all cases, the chosen value of the degree of correlation, say $\frac{Đ_1}{Đ_{12}}$ is on the basis of MD simulations for the specific guest/host combination. In every case, the rationale for the choice of the value of $\frac{Đ_1}{Đ_{12}}$ is provided in the accompanying Figures, on a case-by-case basis.

8. Notation

b_i	parameter in the pure component Langmuir adsorption isotherm, Pa^{-1}
$[B]$	matrix of inverse M-S coefficients, defined by eq. (6), m^{-2} s
c_i	pore concentration of species i, $c_i = q_i / V_p$, mol m^{-3}
$c_{i,sat}$	saturation capacity of species i, mol m^{-3}
c_t	total pore concentration in mixture, mol m^{-3}
D_i	Fick diffusivity of species i, m^2 s^{-1}
$Đ_i$	M-S diffusivity of species i, m^2 s^{-1}
$Đ_{ij}$	M-S exchange coefficient, m^2 s^{-1}
$D_{i,self}$	self-diffusivity of species i, m^2 s^{-1}
f_i	partial fugacity of species i, Pa
p_i	partial pressure of species i in upstream compartment, Pa
p_t	total system pressure in upstream compartment, Pa
q_i	molar loading of species i, mol kg^{-1}
$q_{i,sat}$	molar loading of species i at saturation, mol kg^{-1}
q_t	total molar loading of mixture, mol kg^{-1}
n	number of components in mixture, dimensionless
N_i	molar flux of species i defined in terms of the membrane area, mol m^{-2} s^{-1}
R	gas constant, 8.314 J mol^{-1} K^{-1}
S_{ads}	adsorption selectivity, dimensionless
S_{diff}	diffusion selectivity, dimensionless
S_{perm}	permeation selectivity, dimensionless
T	absolute temperature, K
V_p	pore volume, m^3 kg^{-1}
x_i	mole fraction of species i based on loading within pore, dimensionless
z	distance coordinate, m

Greek letters

δ_{ij}	Kronecker delta, dimensionless
δ	thickness of membrane, m
$[\Delta]$	matrix defined of M-S diffusivities, $m^2\ s^{-1}$
Δ_{ij}	elements of $[\Delta]$, $m^2\ s^{-1}$
$[\Gamma]$	matrix of thermodynamic factors, dimensionless
Γ_{ij}	element of $[\Gamma]$, dimensionless
ϕ	fractional pore volume, dimensionless
Π_i	permeance of species *i* in mixture, mol $m^{-2}\ s^{-1}\ Pa^{-1}$
Π_i^0	permeance of pure component *i*, mol $m^{-2}\ s^{-1}\ Pa^{-1}$
μ_i	molar chemical potential, J mol^{-1}
θ_i	fractional occupancy of component *i*, dimensionless
θ_V	fractional vacancy, dimensionless
Θ_i	loading of species *i*, molecules per unit cell or per cage
$\Theta_{I,sat}$	saturation loading of species *i*, molecules per unit cell or per cage
Θ_t	total molar loading of mixture, molecules per unit cell or per cage
ρ	framework density, kg m^{-3}

Subscripts

i	referring to component *i*
t	referring to total mixture

9. References

[1] A.L. Myers, J.M. Prausnitz, Thermodynamics of mixed gas adsorption, A.I.Ch.E.J. 11 (1965) 121-130.

[2] M.B. Rao, S. Sircar, Thermodynamic consistency for binary gas adsorption equilibria, Langmuir 15 (1999) 7258-7267.

[3] R. Krishna, Describing the diffusion of guest molecules inside porous structures, J. Phys. Chem. C 113 (2009) 19756-19781.

[4] R. Krishna, Diffusion in Porous Crystalline Materials, Chem. Soc. Rev. 41 (2012) 3099-3118.

[5] R. Krishna, J.M. van Baten, Diffusion of alkane mixtures in zeolites. Validating the Maxwell-Stefan formulation using MD simulations, J. Phys. Chem. B 109 (2005) 6386-6396.

[6] R. Krishna, J.M. van Baten, Insights into diffusion of gases in zeolites gained from molecular dynamics simulations, Microporous Mesoporous Mater. 109 (2008) 91-108.

[7] R. Krishna, R. Baur, Modelling issues in zeolite based separation processes, Sep. Purif. Technol. 33 (2003) 213-254.

[8] R. Krishna, D. Paschek, R. Baur, Modelling the occupancy dependence of diffusivities in zeolites, Microporous Mesoporous Mater. 76 (2004) 233-246.

[9] R. Krishna, R. Baur, Diffusion, Adsorption and Reaction in Zeolites: Modelling and Numerical Issues, University of Amsterdam, Amsterdam, http://www.science.uva.nl/research/cr/zeolite/, 11 November 2003.

[10] R. Krishna, R. Baur, Analytic solution of the Maxwell-Stefan equations for multicomponent permeation across a zeolite membrane, Chem. Eng. J. 97 (2004) 37-45.

[11] R. Krishna, J.M. van Baten, Investigating the potential of MgMOF-74 membranes for CO_2 capture, J. Membr. Sci. 377 (2011) 249-260.

[12] R. Krishna, J.M. van Baten, Maxwell-Stefan modeling of slowing-down effects in mixed gas permeation across porous membranes, J. Membr. Sci. 383 (2011) 289-300.

[13] S. Li, J.L. Falconer, R.D. Noble, R. Krishna, Interpreting unary, binary and ternary mixture permeation across a SAPO-34 membrane with loading-dependent Maxwell-Stefan diffusivities, J. Phys. Chem. C 111 (2007) 5075-5082.

10. Listing of Figures containing membrane permeation data and analysis

The structural details, pore landscapes, surface area vs pore size distributions, isotherm fit parameters, and analysis of experimental data on membrane permeation, are presented in the accompanying Figures in the following order:

Cage-type structures with narrow windows

SAPO-34

DDR

ZIF-8

1D micro-porous channels

NiMOF-74

Intersecting channels

MFI

Figure 1

SAPO-34
(structural analog of CHA)

Figure 2

CHA landscape

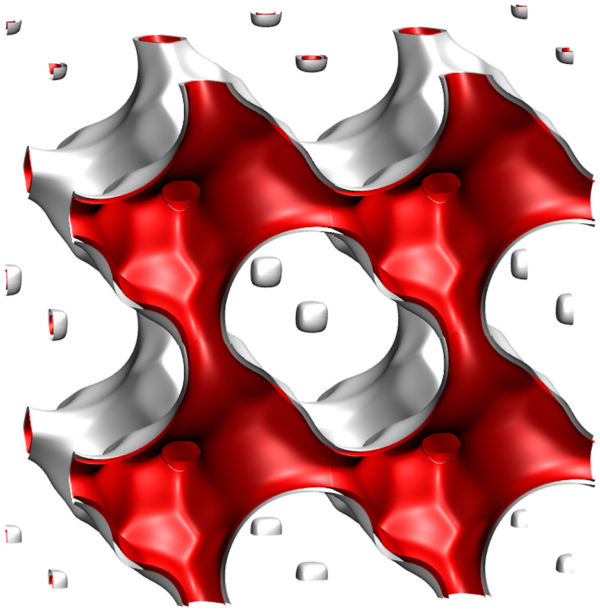

There are 6 cages per unit cell. The volume of one CHA cage is 316.4 Å^3, slightly larger than that of a single cage of DDR (278 Å^3), but significantly lower than FAU (786 Å^3).

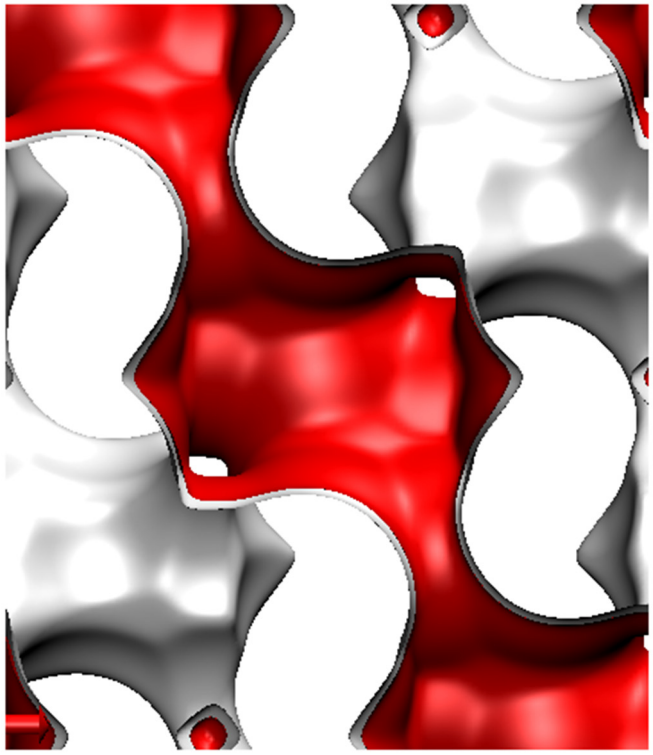

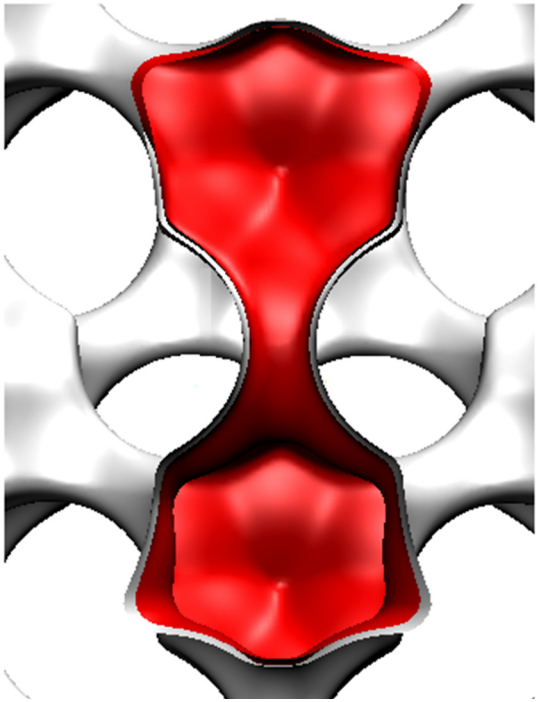

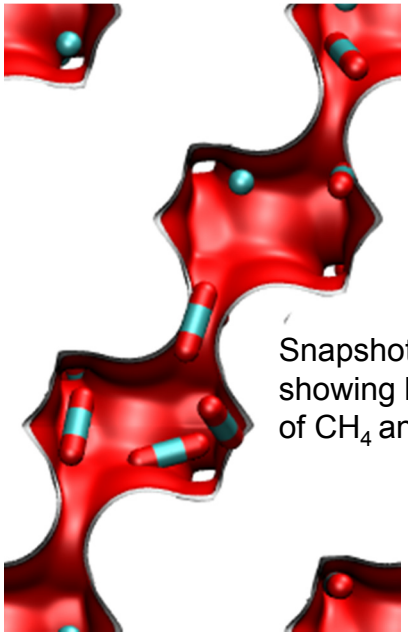

Snapshots showing location of CH_4 and CO_2

Snapshots showing location of CH_4

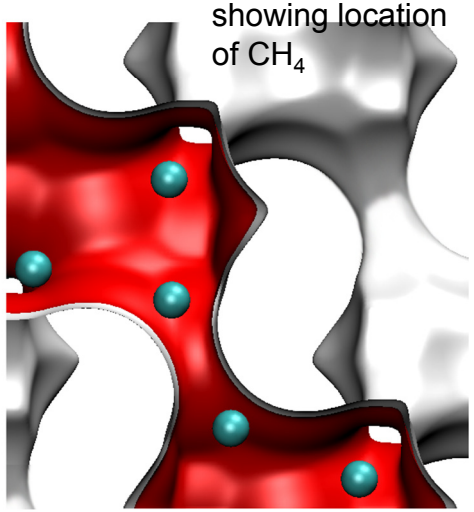

Structural information from: C. Baerlocher, L.B. McCusker, Database of Zeolite Structures, International Zeolite Association, http://www.iza-structure.org/databases/

CHA window and pore dimensions

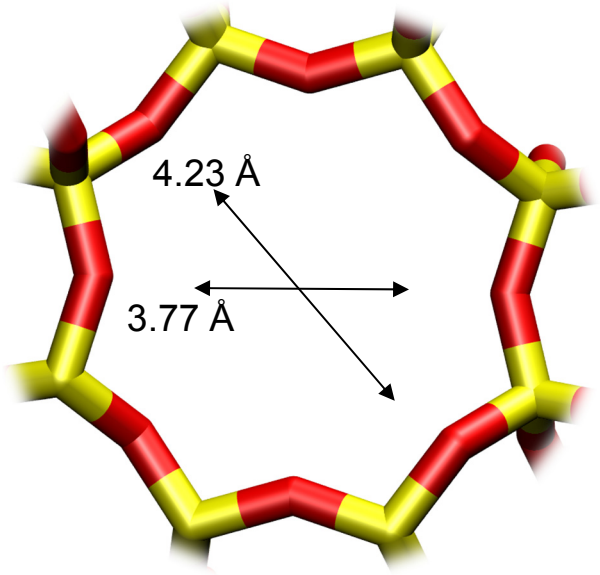

CHA

The window dimensions calculated using the van der Waals diameter of framework atoms = 2.7 Å are indicated above by the arrows.

This plot of surface area versus pore dimension is determined using a combination of the DeLaunay triangulation method for pore dimension determination, and the procedure of Düren for determination of the surface area.

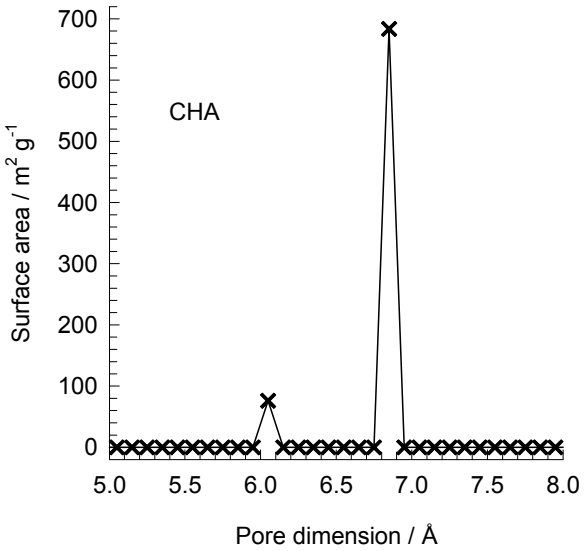

	CHA
a /Å	15.075
b /Å	23.907
c /Å	13.803
Cell volume / Å^3	4974.574
conversion factor for [molec/uc] to [mol per kg Framework]	0.2312
conversion factor for [molec/uc] to [kmol/m^3]	0.8747
ρ [kg/m3]	1444.1
MW unit cell [g/mol(framework)]	4326.106
ϕ, fractional pore volume	0.382
open space / Å^3/uc	1898.4
Pore volume / cm^3/g	0.264
Surface area /m^2/g	758.0
DeLaunay diameter /Å	3.77

SAPO-34 fits of experimental isotherms for pure components

Figure 4

Pure component isotherm fit data for SAPO-34 are fitted using the statistical isotherm

$$q_i = \frac{q_{i,sat}}{\Omega_i} \frac{b_i f_i + \sum_{m=2}^{\Omega_i} \frac{(b_i f_i)^m}{(m-1)!} \left[\frac{1 - \frac{m}{\Omega_i + 1}}{1 - \frac{1}{\Omega_i + 1}} \right]^m}{1 + b_i f_i + \sum_{m=2}^{\Omega_i} \frac{(b_i f_i)^m}{(m)!} \left[\frac{1 - \frac{m}{\Omega_i + 1}}{1 - \frac{1}{\Omega_i + 1}} \right]^m}$$

Molecule	b_i	Ω_i	$q_{i,sat}$
CO_2	7.67×10^{-5}	6	8.2
CH_4	5.87×10^{-6}	6	8.2
N_2	1.26×10^{-6}	6	8.2
H_2	2.84×10^{-7}	9	12.3
O_2	1.2×10^{-6}	6	8.2
CO	2.31×10^{-6}	6	8.2
Ar	1.26×10^{-6}	6	8.2

b_i is expressed in Pa^{-1}, Ω_i in molecules per cage, $q_{i,sat}$ in mol kg^{-1}.

The original data is from:

S. Li, J.L. Falconer, R.D. Noble, R. Krishna, Interpreting unary, binary and ternary mixture permeation across a SAPO-34 membrane with loading-dependent Maxwell-Stefan diffusivities, J. Phys. Chem. C 111 (2007) 5075-5082.

Figure 5

SAPO-34: Snapshots of CO_2/CH_4 mixtures

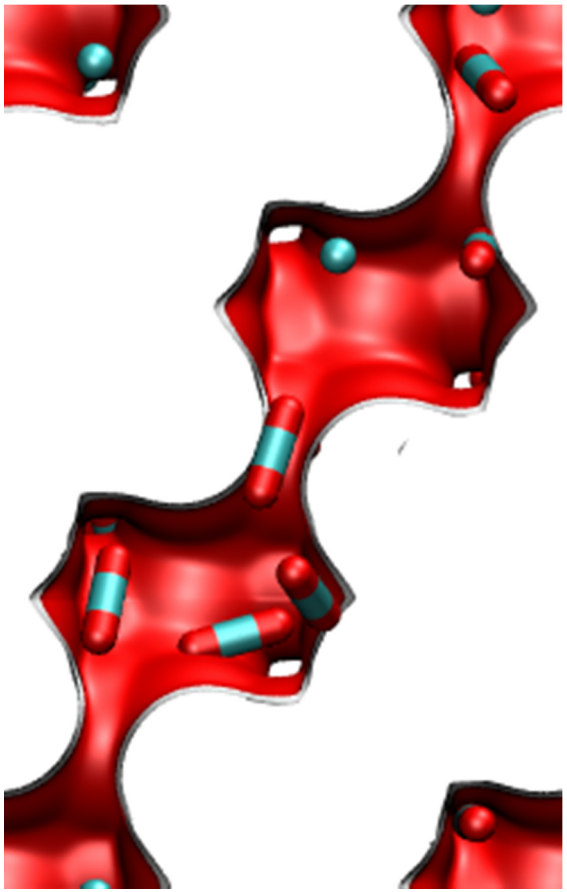

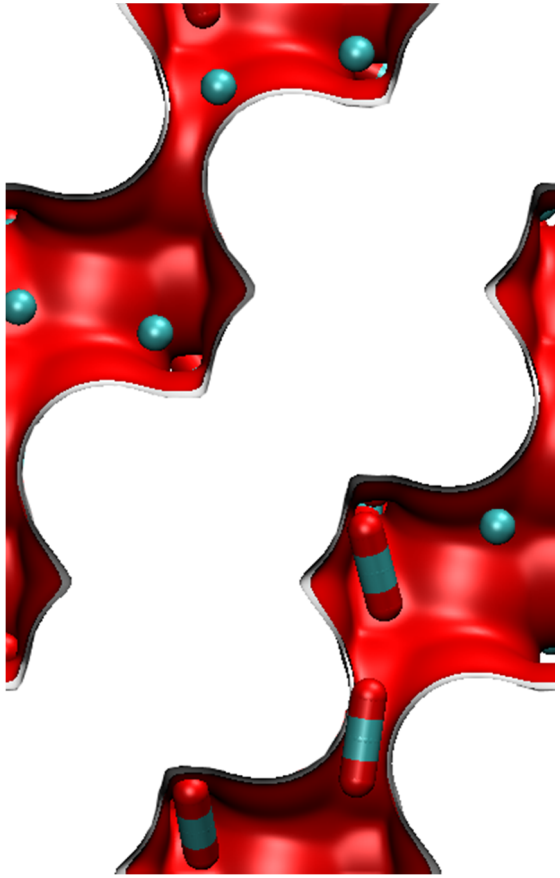

SAPO-34: Maxwell-Stefan model calculations for CO_2/CH_4 mixture permeation

Figure 6

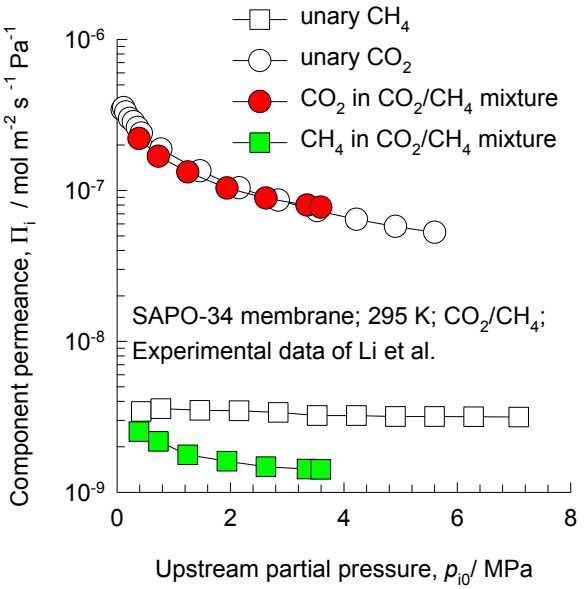

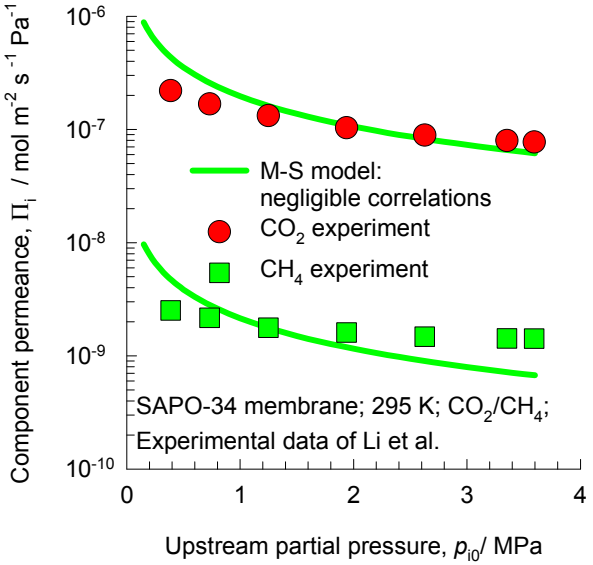

The inputs for the Maxwell-Stefan model are:

$$\frac{\rho Đ_1}{\delta} = 0.035 \ \text{kg m}^{-2} \ \text{s}^{-1}$$

$$\frac{\rho Đ_2}{\delta} = 0.005 \ \text{kg m}^{-2} \ \text{s}^{-1}$$

In the M-S model calculations, correlations are considered to be negligible

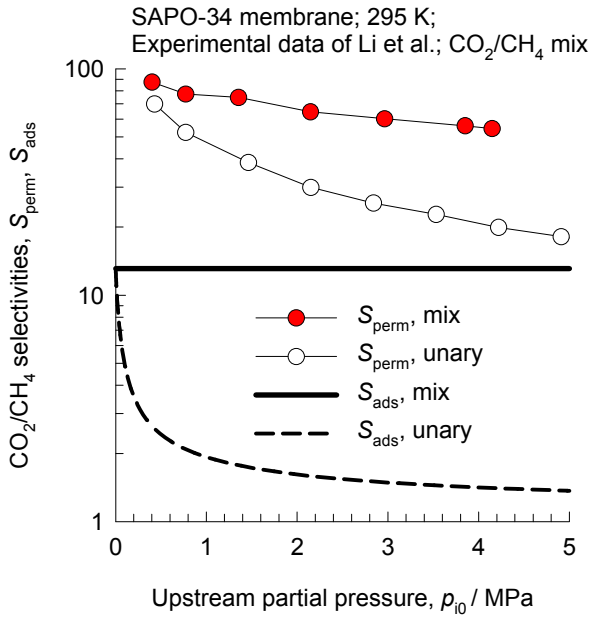

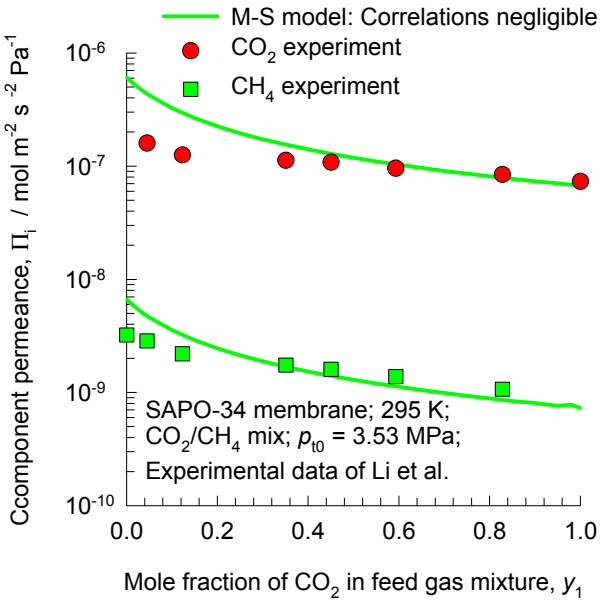

The same parameter inputs, as specified above, are equally good in estimation of component permeances when the composition of the feed mixture is varied, keeping the total upstream pressure = 3.53 MPa

Figure 7

SAPO-34: Snapshots of CO_2/H_2 mixtures

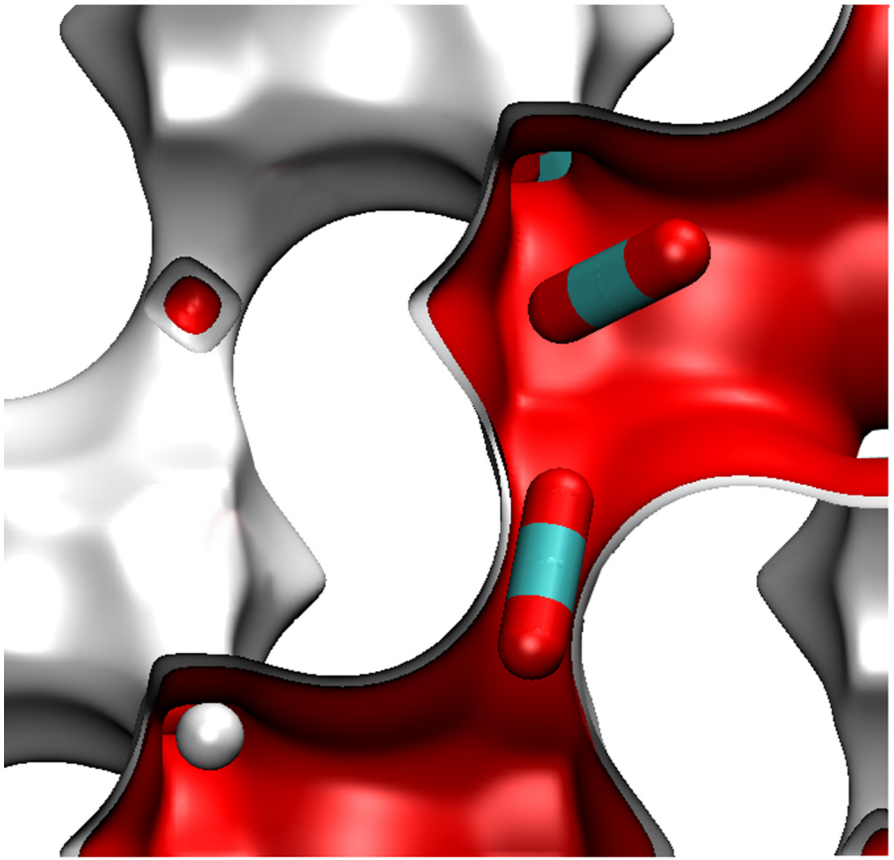

SAPO-34: Maxwell-Stefan model calculations for H_2/CO_2 mixture permeation

Figure 8

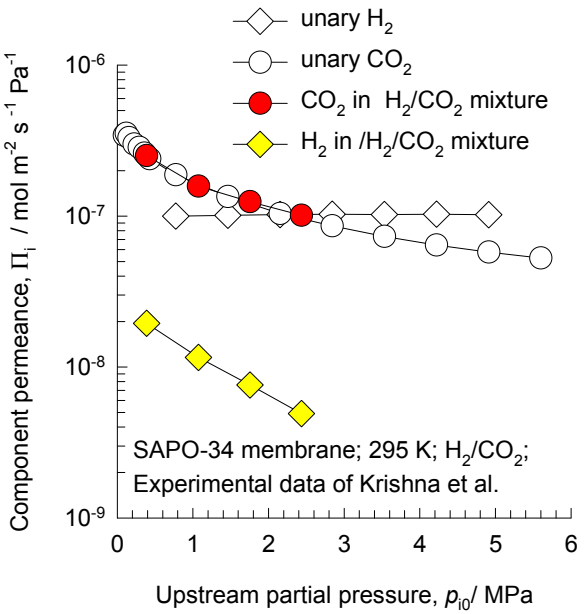

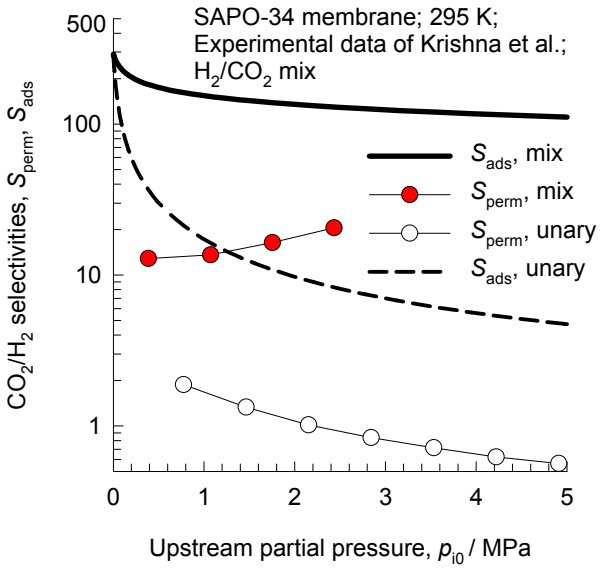

The inputs for the Maxwell-Stefan model are:

$$\frac{\rho Đ_1}{\delta} = 0.3 \ \text{kg m}^{-2} \ \text{s}^{-1}$$

$$\frac{\rho Đ_2}{\delta} = 0.035 \ \text{kg m}^{-2} \ \text{s}^{-1}$$

In the M-S model calculations, correlations are considered to be negligible

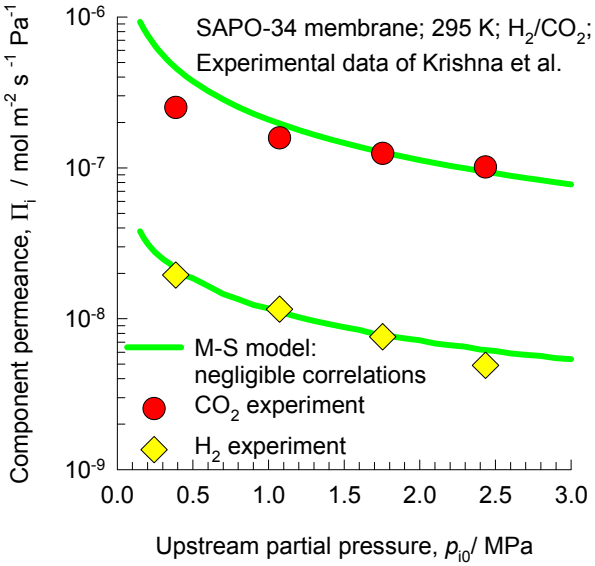

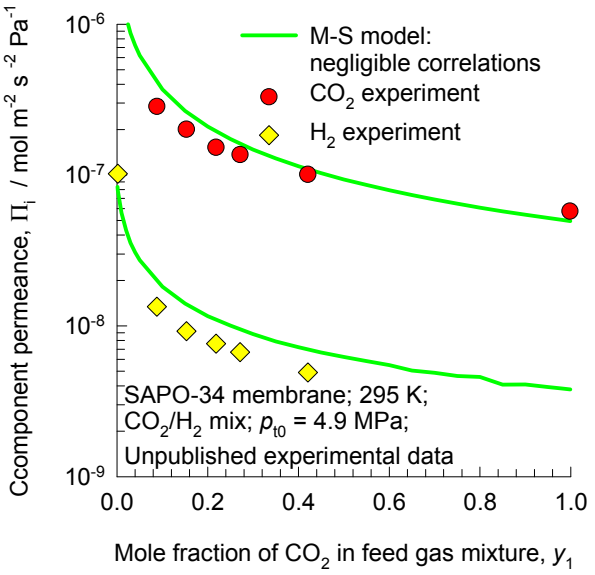

The same parameter inputs, as specified above, are equally good in estimation of component permeances when the composition of the feed mixture is varied, keeping the total upstream pressure = 4.9 MPa

SAPO-34 CO_2/N_2 mixture permeances, compared with unary permeances

Figure 9

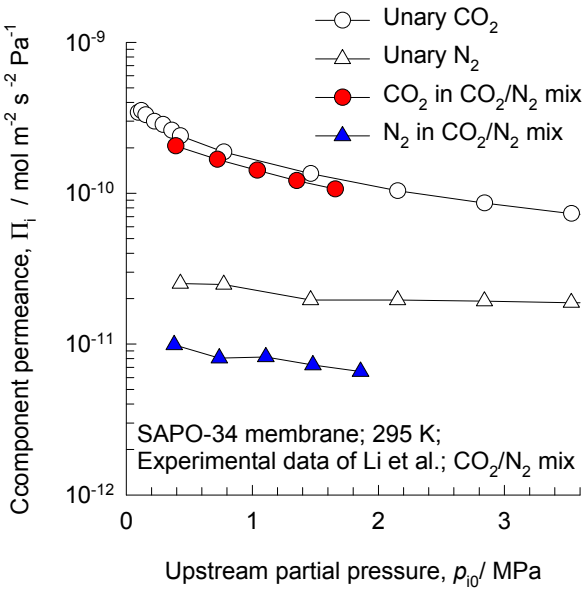

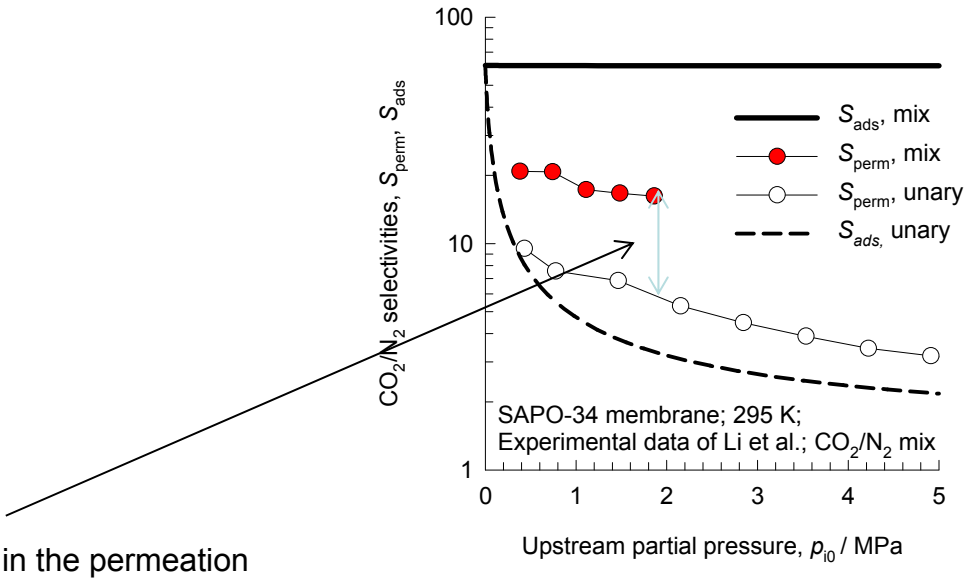

The increase in the permeation selectivity in the mixture is due primarily to the stronger adsorption selectivity. Correlation effects are not of major importance for this system.

The data are re-plotted using the information in:
S. Li, J.L. Falconer, R.D. Noble, R. Krishna, Interpreting unary, binary and ternary mixture permeation across a SAPO-34 membrane with loading-dependent Maxwell-Stefan diffusivities, J. Phys. Chem. C 111 (2007) 5075-5082

SAPO-34 CH_4/H_2 mixture permeances, compared with unary permeances

Figure 10

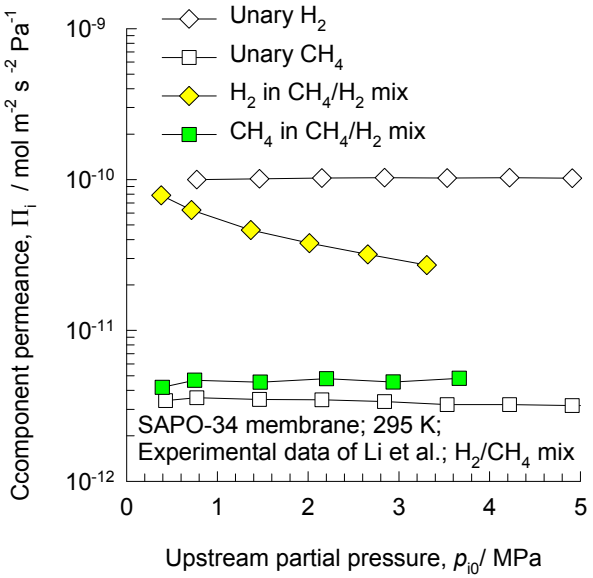

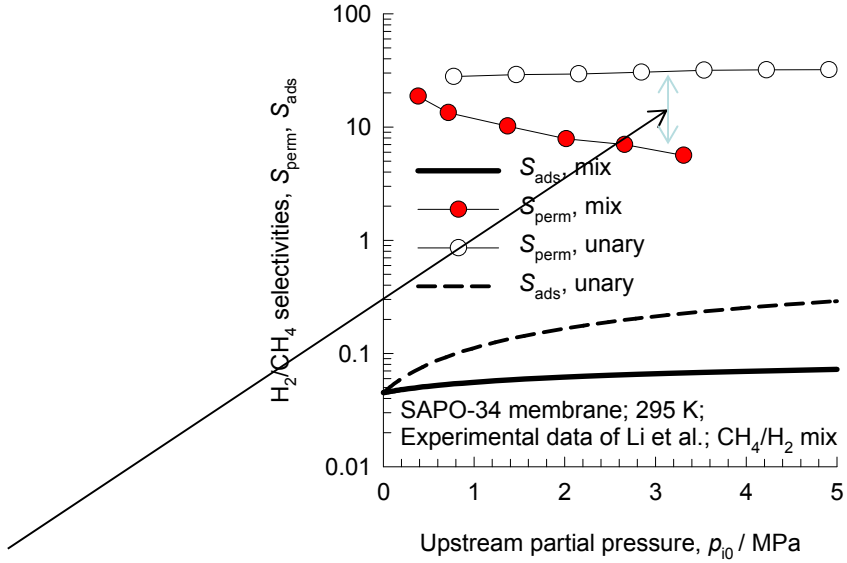

The reduction in the permeation selectivity in the mixture is due primarily to the decrease in adsorption selectivity. Correlation effects are not of major importance for this system.

The data are re-plotted using the information in:
S. Li, J.L. Falconer, R.D. Noble, R. Krishna, Interpreting unary, binary and ternary mixture permeation across a SAPO-34 membrane with loading-dependent Maxwell-Stefan diffusivities, J. Phys. Chem. C 111 (2007) 5075-5082

SAPO-34 CH_4/N_2 mixture permeances, compared with unary permeances

Figure 11

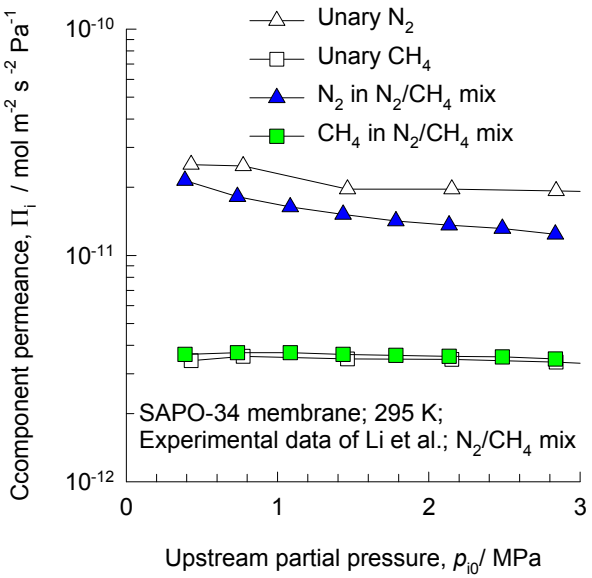

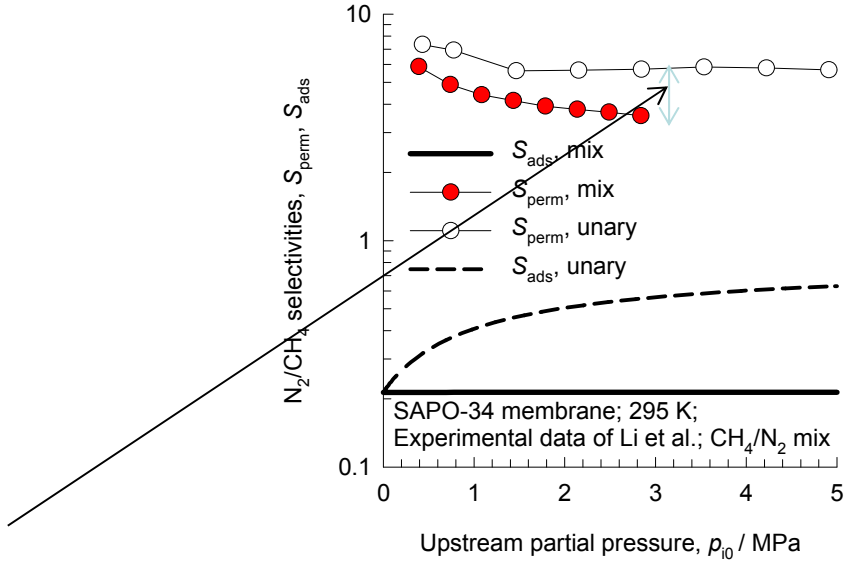

The reduction in the permeation selectivity in the mixture is due primarily to the decrease in adsorption selectivity. Correlation effects are not of major importance for this system.

The data are re-plotted using the information in:
S. Li, J.L. Falconer, R.D. Noble, R. Krishna, Interpreting unary, binary and ternary mixture permeation across a SAPO-34 membrane with loading-dependent Maxwell-Stefan diffusivities, J. Phys. Chem. C 111 (2007) 5075-5082

SAPO-34 CH_4/Ar mixture permeances, compared with unary permeances

Figure 12

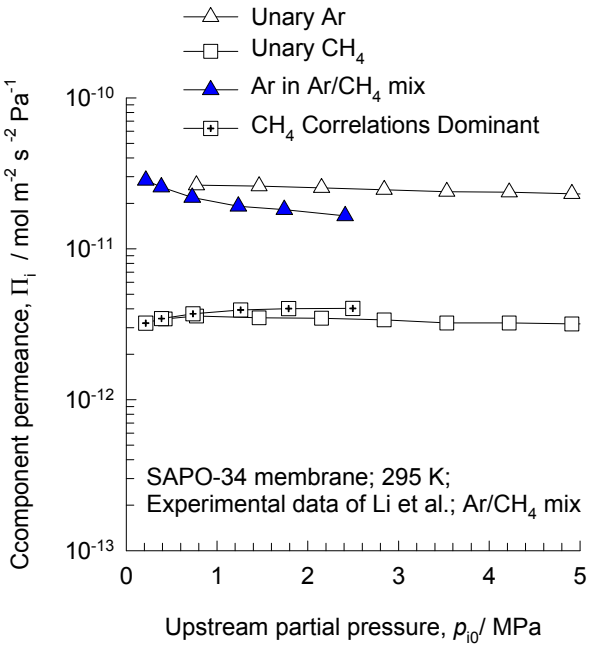

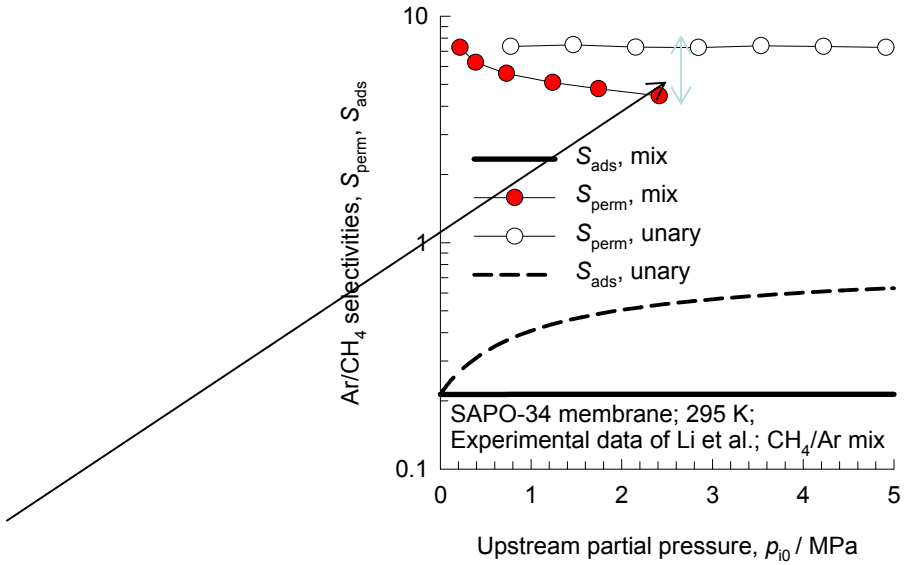

The reduction in the permeation selectivity in the mixture is due primarily to the decrease in adsorption selectivity. Correlation effects are not of major importance for this system.

The data are re-plotted using the information in:
S. Li, J.L. Falconer, R.D. Noble, R. Krishna, Interpreting unary, binary and ternary mixture permeation across a SAPO-34 membrane with loading-dependent Maxwell-Stefan diffusivities, J. Phys. Chem. C 111 (2007) 5075-5082

SAPO-34 N_2/H_2 mixture permeances, compared with unary permeances

Figure 13

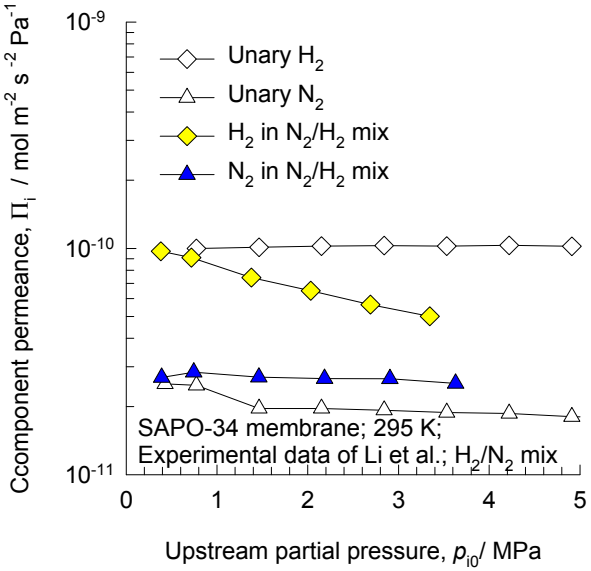

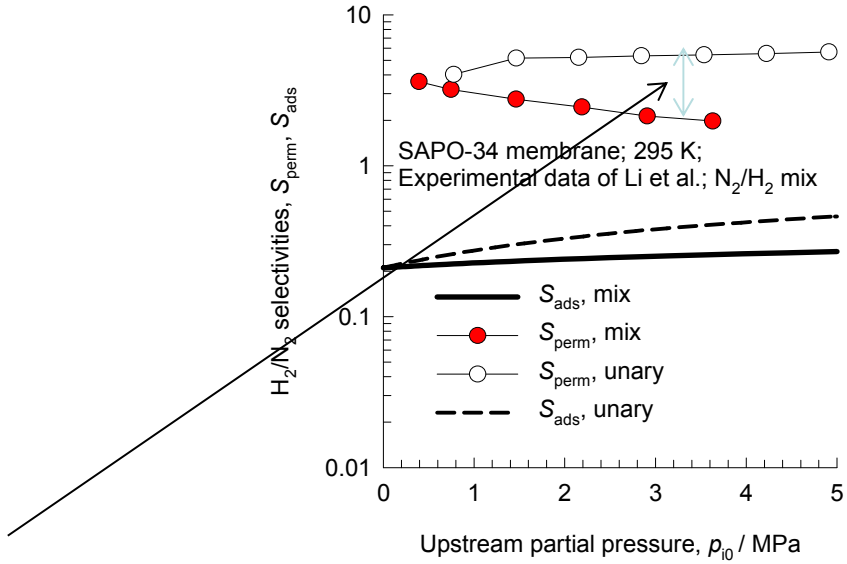

The reduction in the permeation selectivity in the mixture is due primarily to the decrease in adsorption selectivity. Correlation effects are not of major importance for this system.C

The data are re-plotted using the information in:
S. Li, J.L. Falconer, R.D. Noble, R. Krishna, Interpreting unary, binary and ternary mixture permeation across a SAPO-34 membrane with loading-dependent Maxwell-Stefan diffusivities, J. Phys. Chem. C 111 (2007) 5075-5082

SAPO-34 CO_2 permeance: influence of partner species

Figure 14

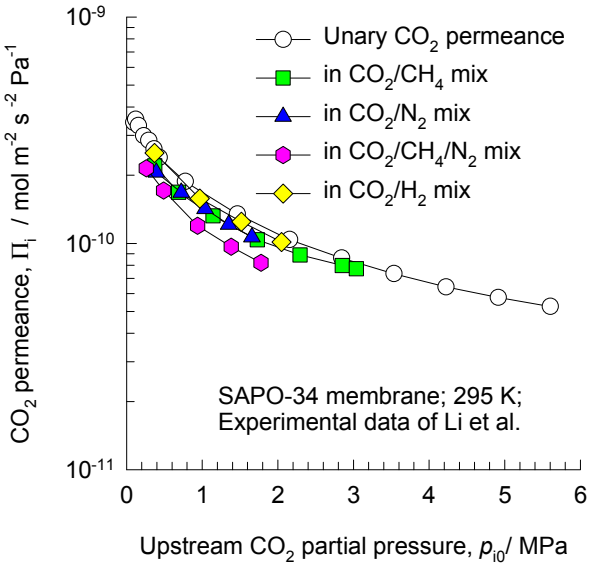

The permeance of CO_2 is practically unchanged as the partner molecules are changed. Correlations effects are not of importance for the more strongly adsorbed species.

The data are re-plotted using the information in:
S. Li, J.L. Falconer, R.D. Noble, R. Krishna, Interpreting unary, binary and ternary mixture permeation across a SAPO-34 membrane with loading-dependent Maxwell-Stefan diffusivities, J. Phys. Chem. C 111 (2007) 5075-5082

Figure 15

DDR
(all-silica)

DDR landscape

Figure 16

There are 12 cages per unit cell. The volume of one DDR cage is 278 Å^3, significantly smaller than that of a single cage of FAU (786 Å^3), or ZIF-8 (1168 Å^3).

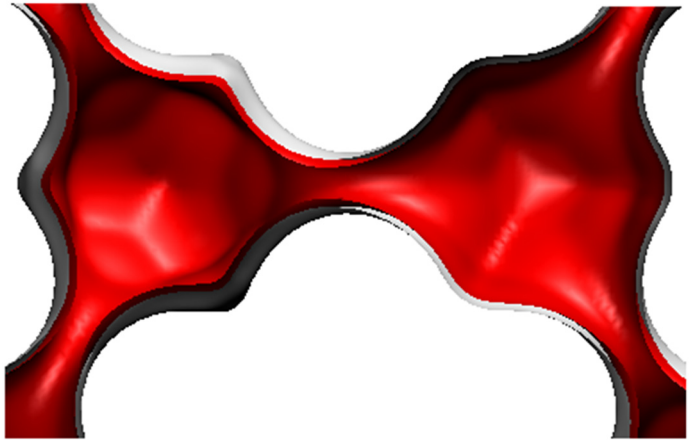

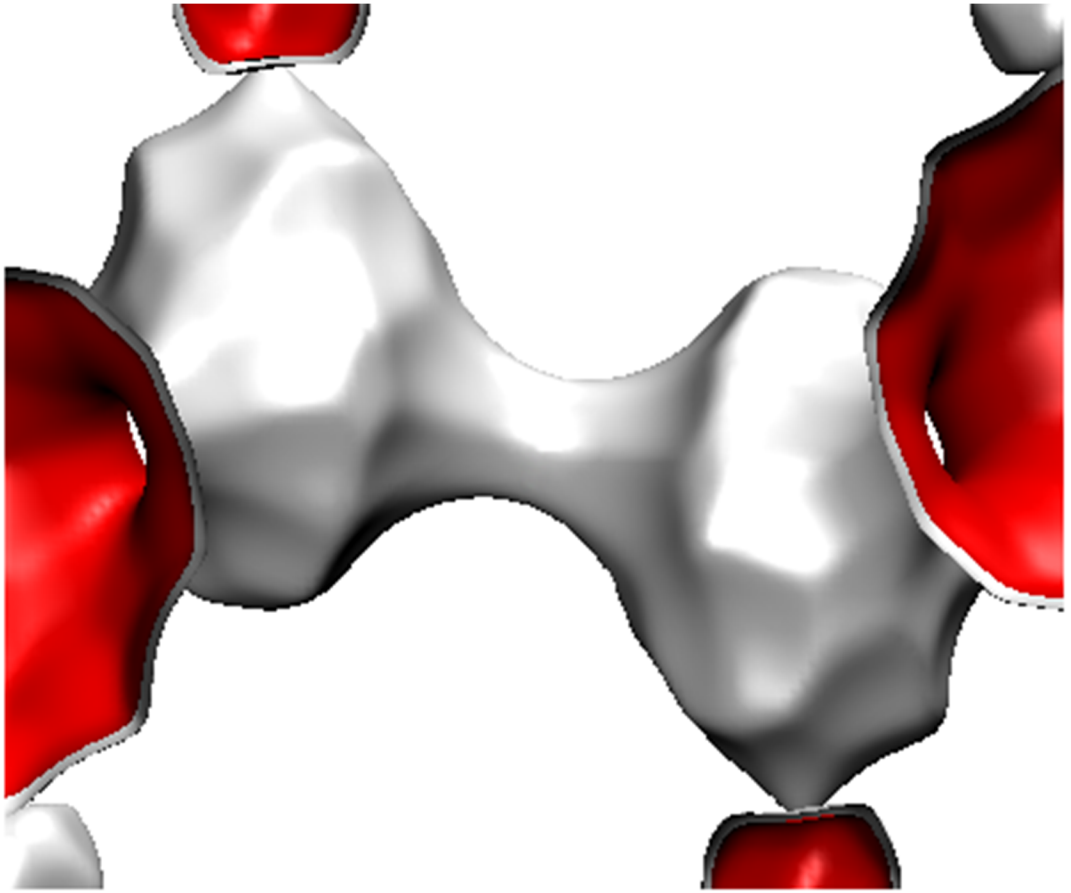

Structural information from: C. Baerlocher, L.B. McCusker, Database of Zeolite Structures, International Zeolite Association, http://www.iza-structure.org/databases/

DDR window and pore dimensions

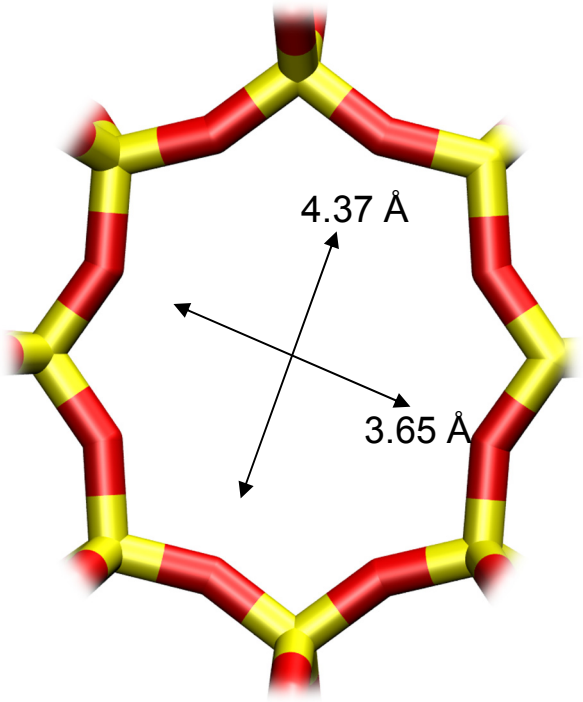

DDR

The window dimensions calculated using the van der Waals diameter of framework atoms = 2.7 Å are indicated above by the arrows.

This plot of surface area versus pore dimension is determined using a combination of the DeLaunay triangulation method for pore dimension determination, and the procedure of Düren for determination of the surface area.

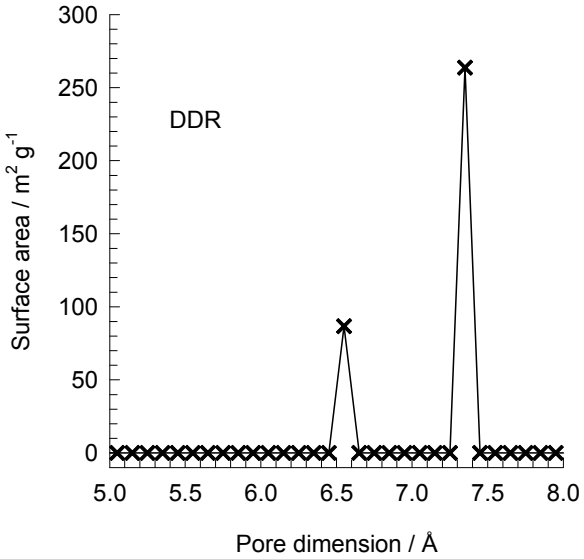

	DDR
a /Å	24.006
b /Å	13.86
c /Å	40.892
Cell volume / Å^3	13605.72
conversion factor for [molec/uc] to [mol per kg Framework]	0.0693
conversion factor for [molec/uc] to [kmol/m^3]	0.4981
ρ [kg/m3]	1759.991
MW unit cell [g/mol(framework)]	14420.35
ϕ, fractional pore volume	0.245
open space / Å^3/uc	3333.5
Pore volume / cm^3/g	0.139
Surface area /m^2/g	350.0
DeLaunay diameter /Å	3.65

DDR snapshots of CO_2/CH_4 mixture

Figure 18

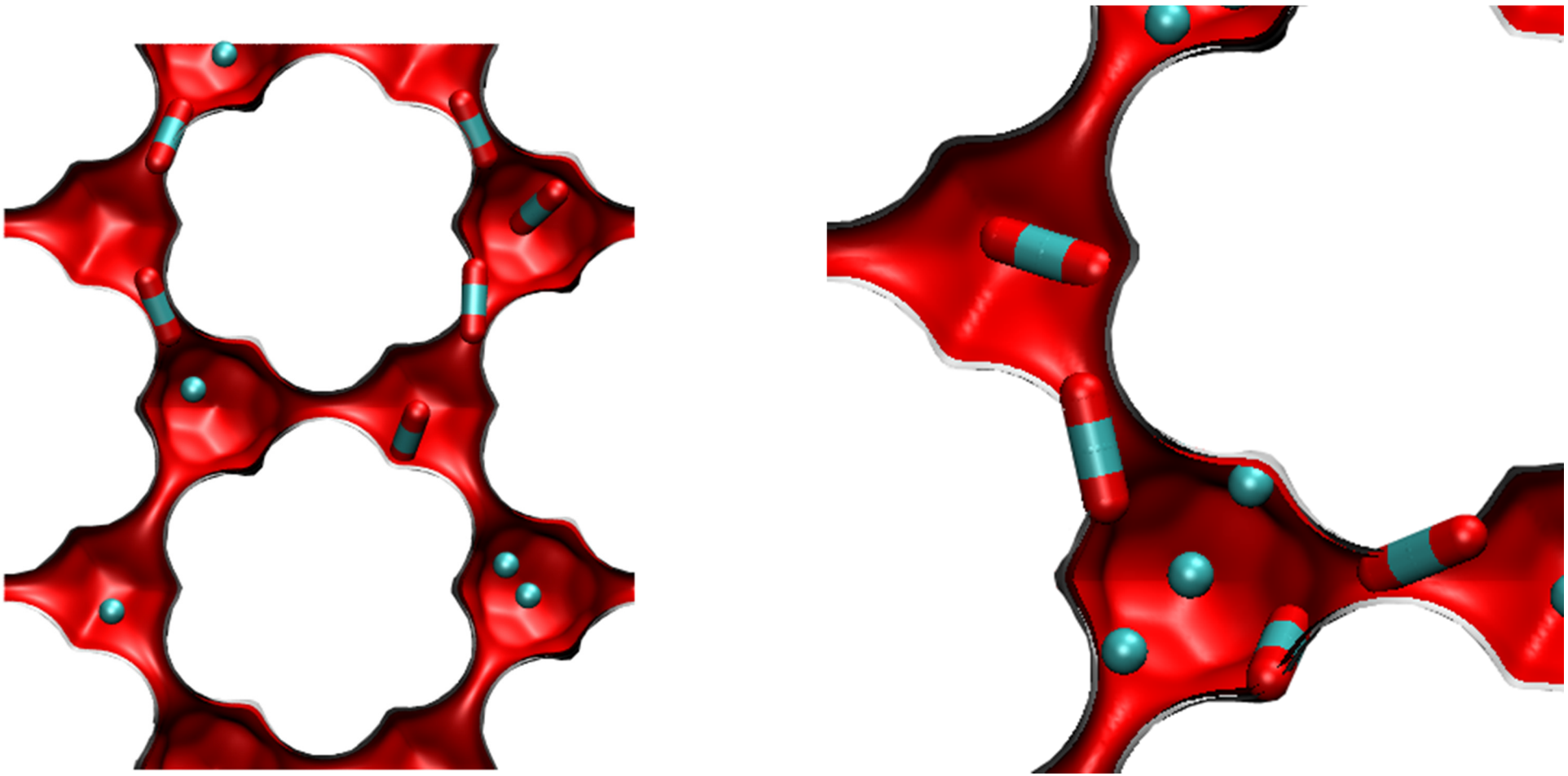

DDR CO_2/CH_4 mixture permeances, compared with unary permeances

Figure 19

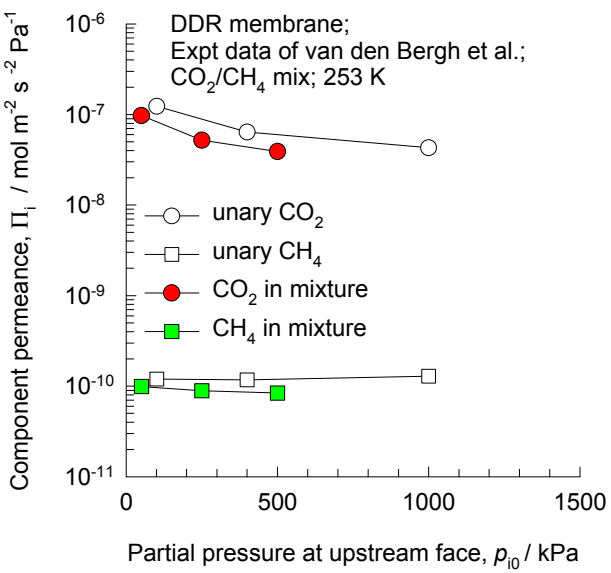

The permeance of each species remains practically unchanged in the mixture. This indicates that correlation effects are not significant.

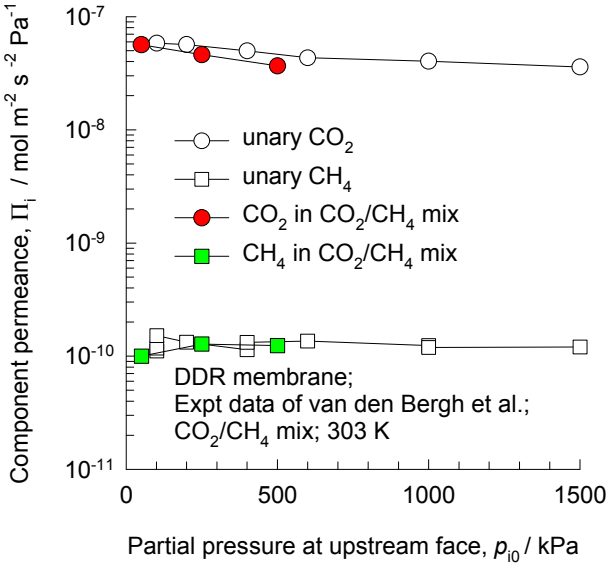

The experimental data are from:
J. van den Bergh, W. Zhu, J. Gascon, J.A. Moulijn, F. Kapteijn, Separation and Permeation Characteristics of a DD3R Zeolite Membrane, J. Membr. Sci. 316 (2008) 35-45.

J. van den Bergh, W. Zhu, J.C. Groen, F. Kapteijn, J.A. Moulijn, K. Yajima, K. Nakayama, T. Tomita, S. Yoshida, Natural Gas Purification with a DDR Zeolite Membrane; Permeation Modelling with Maxwell-Stefan Equations, Stud. Surf. Sci. Catal. 170 (2007) 1021-1027.

Figure 20

DDR Transport coefficients: unary vs mixture

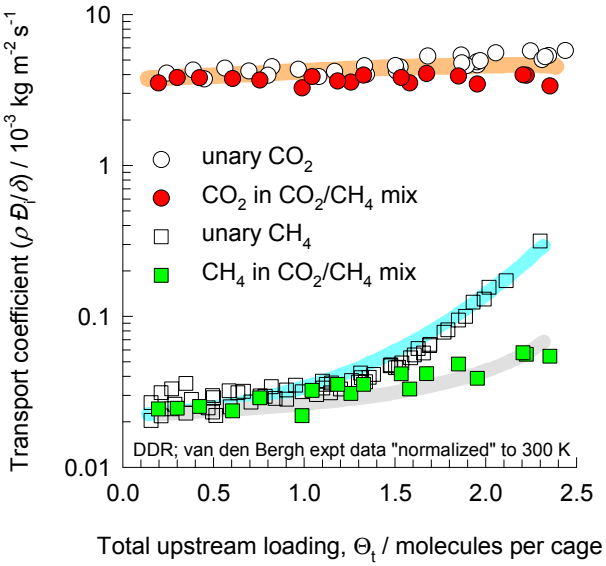

A more detailed analysis of the permeation experiments reveals that the transport of CH_4 in the mixture is hindered due to the preponderance of CO_2 molecules lodged at the window sites.

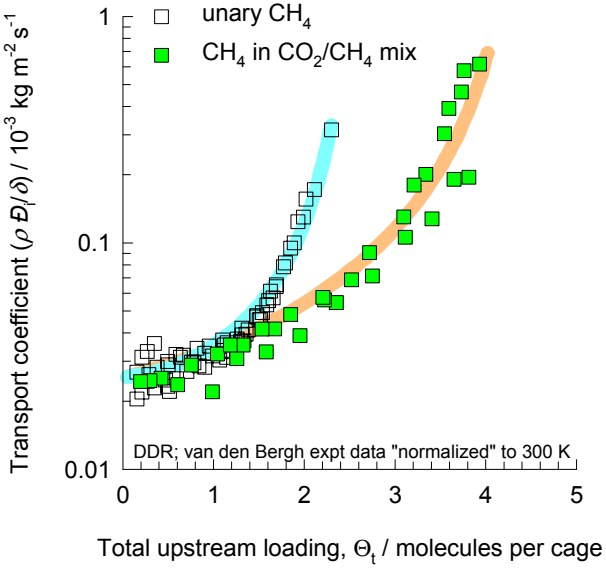

The experimental data are from:
J. van den Bergh, W. Zhu, J. Gascon, J.A. Moulijn, F. Kapteijn, Separation and Permeation Characteristics of a DD3R Zeolite Membrane, J. Membr. Sci. 316 (2008) 35-45.
J. van den Bergh, W. Zhu, J.C. Groen, F. Kapteijn, J.A. Moulijn, K. Yajima, K. Nakayama, T. Tomita, S. Yoshida, Natural Gas Purification with a DDR Zeolite Membrane; Permeation Modelling with Maxwell-Stefan Equations, Stud. Surf. Sci. Catal. 170 (2007) 1021-1027.

These data were modeled using the Maxwell-Stefan diffusion equations, along with Reed & Ehrlich model for the concentration dependence of the M-S diffusivities. The modeling work is reported in our previous works:
R. Krishna, J.M. van Baten, Onsager coefficients for binary mixture diffusion in nanopores, Chem. Eng. Sci. 63 (2008) 3120-3140.
R. Krishna, J.M. van Baten, Segregation effects in adsorption of CO2 containing mixtures and their consequences for separation selectivities in cage-type zeolites, Sep. Purif. Technol. 61 (2008) 414-423.
R. Krishna, J.M. van Baten, A molecular dynamics investigation of a variety of influences of temperature on diffusion in zeolites, Microporous Mesoporous Mater. 125 (2009) 126-134.
C. Chmelik, R. Krishna, Hindering effects in CO_2/CH_4 mixture diffusion in ZIF-8 crystals, J. Membr. Sci. 397-398 (2012) 87-91.

Figure 21

ZIF-8

ZIF-8 pore landscapes

The ZIF-8 = Zn(methylimidazole)$_2$ structure was taken from
R. Banerjee, A. Phan, B. Wang, C. Knobler, H. Furukawa, M. O'Keeffe, O.M. Yaghi, High-Throughput Synthesis of Zeolitic Imidazolate Frameworks and Application to CO_2 Capture, Science 319 (2008) 939-943.
The original structural data (cif file) contains solvent molecules; these were removed and the solvent-free structures were simulated.

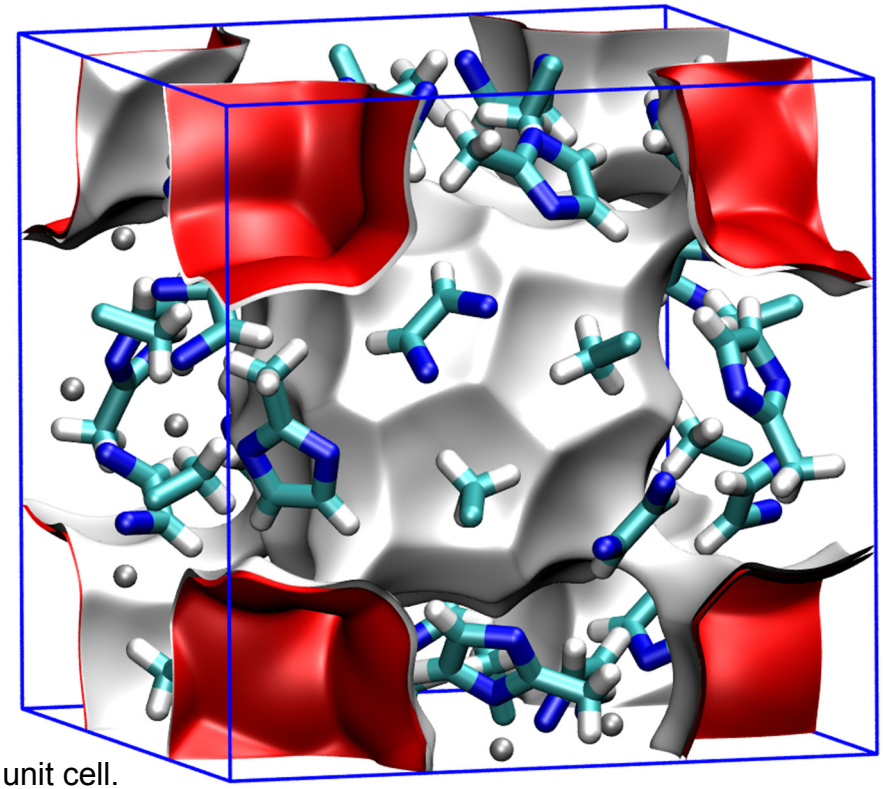

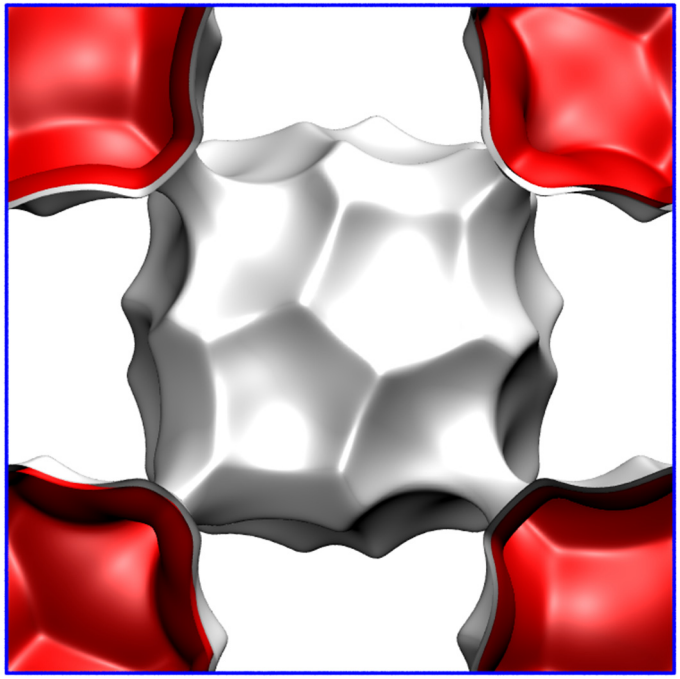

There are 2 cages per unit cell. The volume of one ZIF-8 cage is 1168 Å^3, significantly larger than that of a single cage of DDR (278 Å^3), or FAU (786 Å^3).

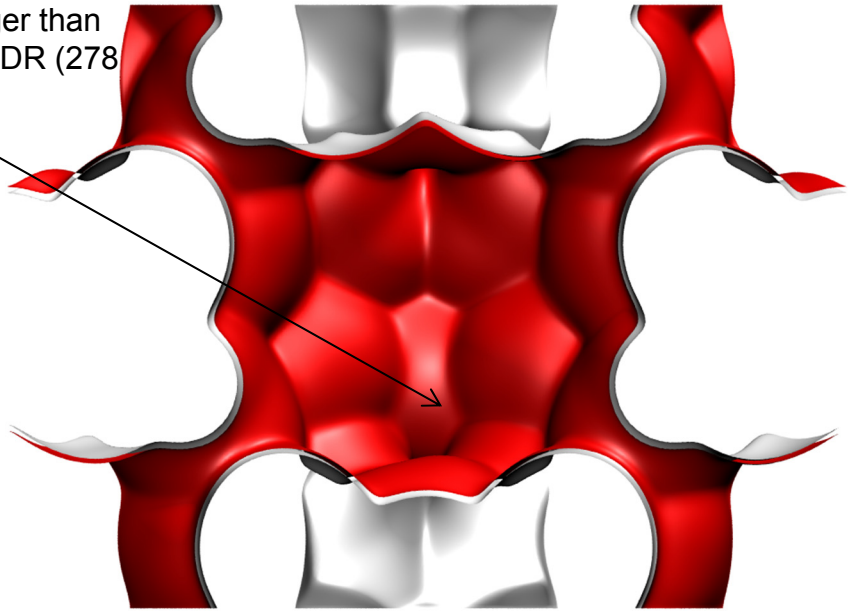

ZIF-8 dimensions

Figure 23

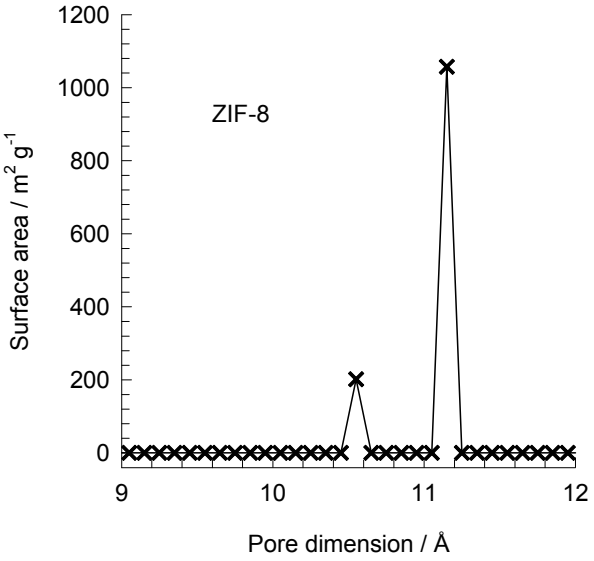

This plot of surface area versus pore dimension is determined using a combination of the DeLaunay triangulation method for pore dimension determination, and the procedure of Düren for determination of the surface area.

	ZIF-8
a /Å	16.991
b /Å	16.991
c /Å	16.991
Cell volume / Å^3	4905.201
conversion factor for [molec/uc] to [mol per kg Framework]	0.3663
conversion factor for [molec/uc] to [kmol/m^3]	0.7106
ρ [kg/m3]	924.253
MW unit cell [g/mol(framework)]	2730.182
ϕ, fractional pore volume	0.476
open space / Å^3/uc	2337.0
Pore volume / cm^3/g	0.515
Surface area /m^2/g	1164.7
DeLaunay diameter /Å	3.26

ZIF-8 snapshot of CO_2/CH_4 mixture

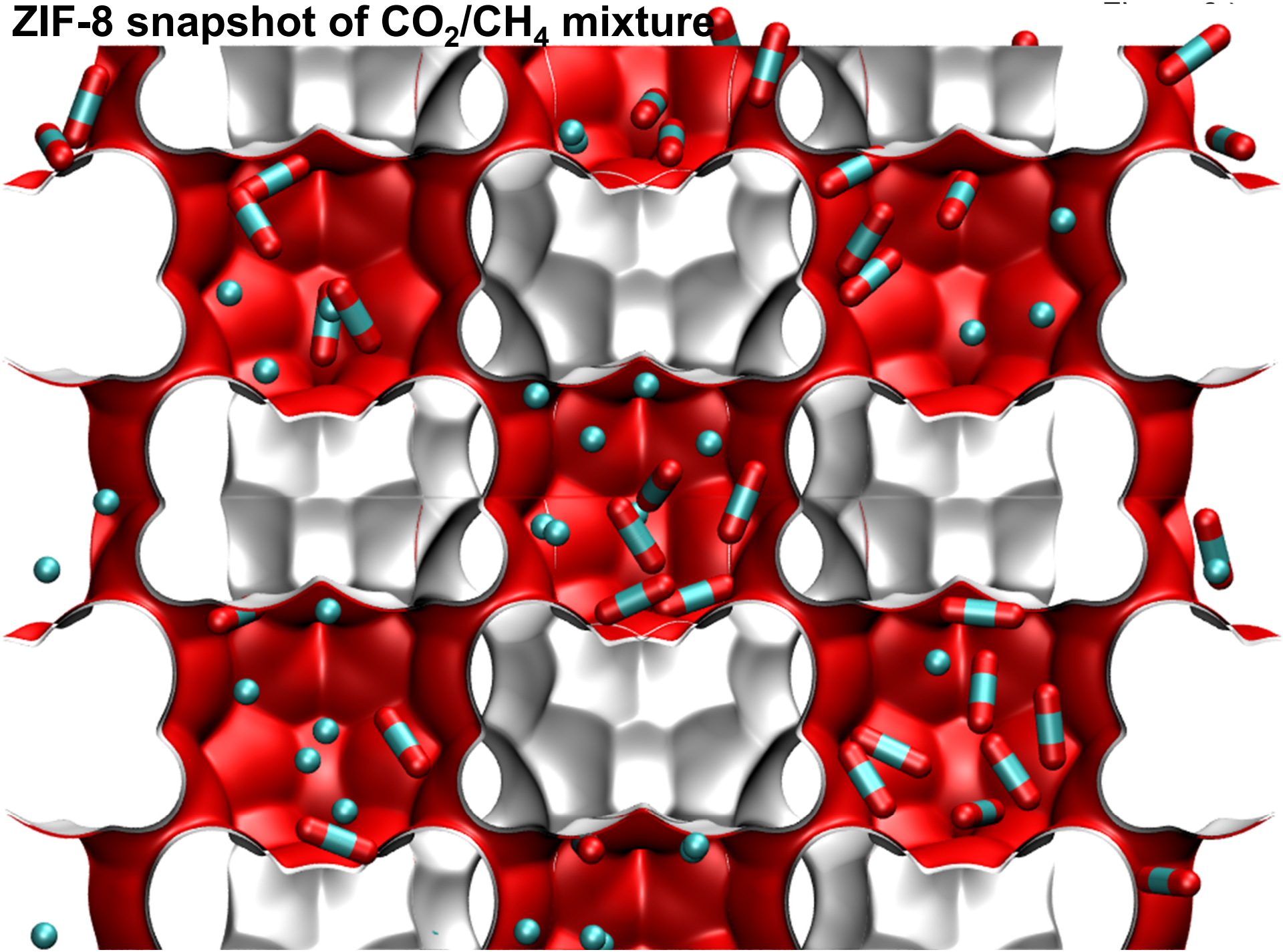

ZIF-8 pure component isotherms; comparison with experiments

Figure 25

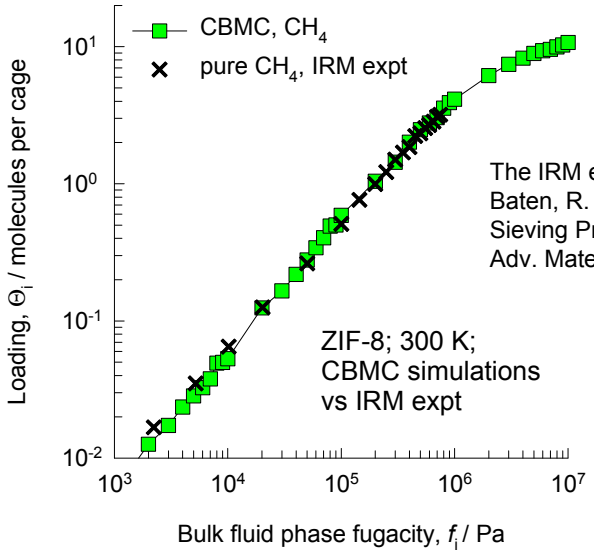

The IRM experimental data is from H. Bux, C. Chmelik, J.M. Van Baten, R. Krishna, J. Caro, Novel MOF-Membrane for Molecular Sieving Predicted by IR-Diffusion Studies and Molecular Modeling, Adv. Mater. 22 (2010) 4741-4743.

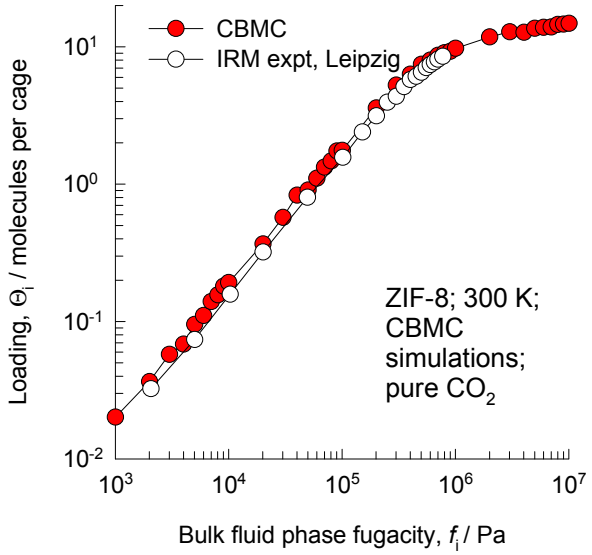

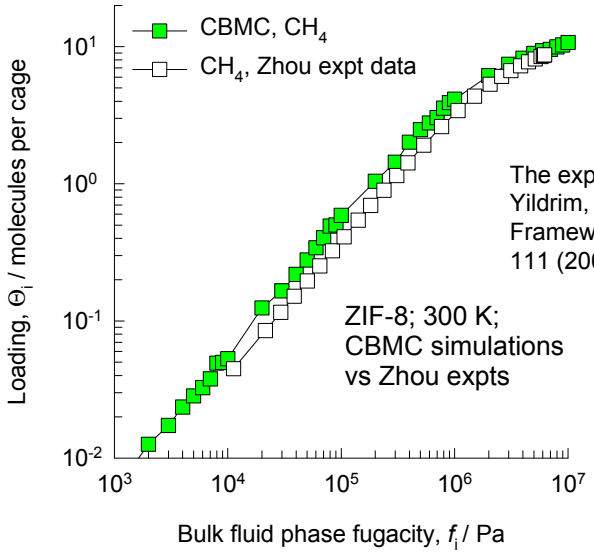

The experimental data is from W. Zhou, H. Wu, M.R. Hartman, T. Yildrim, Hydrogen and Methane Adsorption in Metal-Organic Frameworks: A High-Pressure Volumetric Study, J. Phys. Chem. C 111 (2007) 16131-16137.

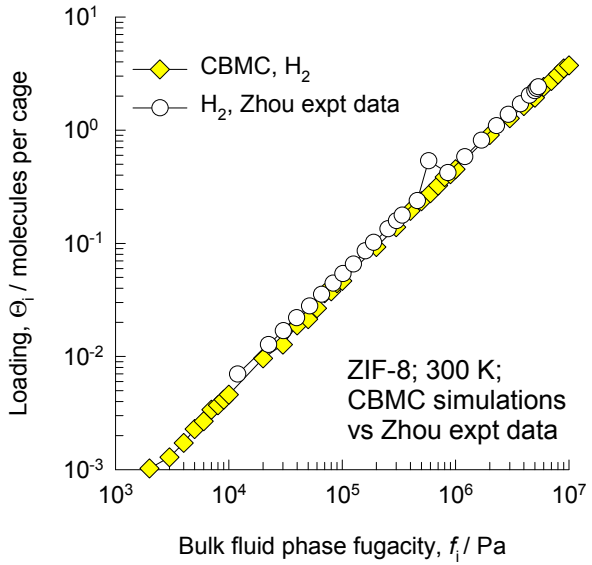

ZIF-8 pure component isotherms; comparison with experiments

Figure 26

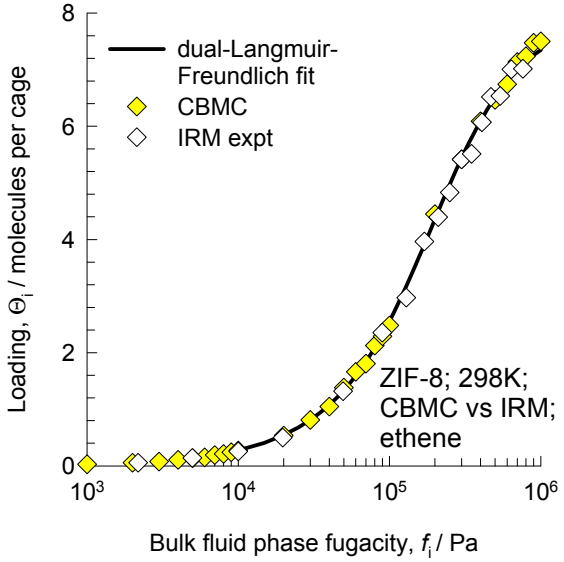

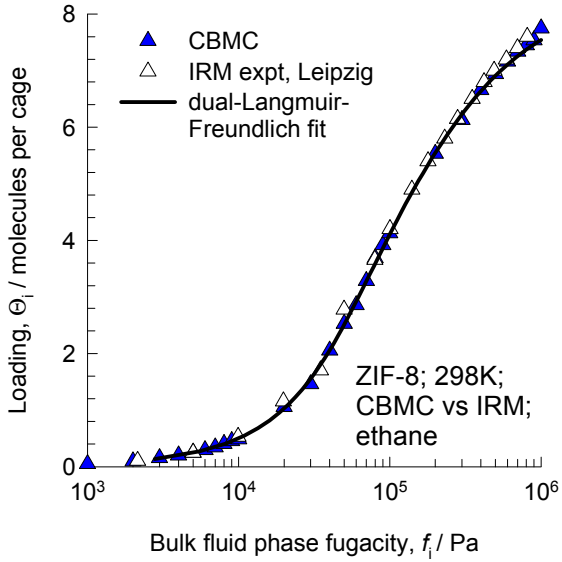

The IRM experimental data is from H. Bux, C. Chmelik, R. Krishna, J. Caro, Ethene/Ethane Separation by the MOF Membrane ZIF-8: Molecular Correlation of Permeation, Adsorption, Diffusion, J. Membr. Sci. 369 (2011) 284-289.

ZIF-8 Fitting parameters for pure component isotherms determined from CBMC simulations

Figure 27

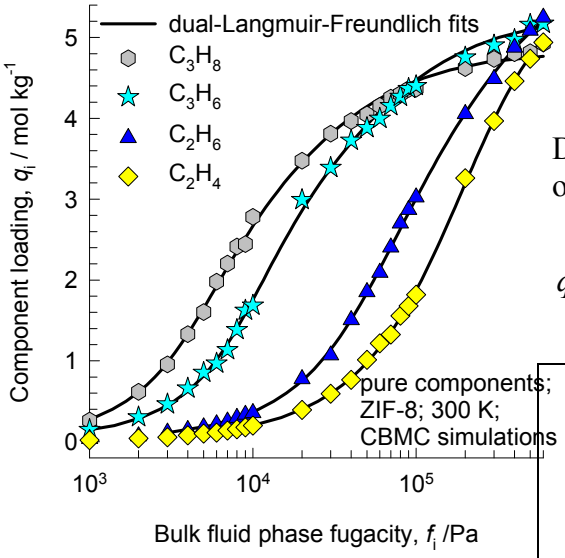

Dual-site Langmuir-Freundlich parameters for pure components in ZIF-8 at 300 K These fits are based on CBMC simulations.

$$q_i = q_{i,A,sat}\frac{b_{i,A}f_i^{\nu_A}}{1+b_{i,A}f_i^{\nu_A}} + q_{i,B,sat}\frac{b_{i,B}f_i^{\nu_B}}{1+b_{i,B}f_i^{\nu_B}}$$

	Site A			Site B		
	$q_{i,A,sat}$ mol/kg	$b_{i,A}$ $Pa^{-\nu_i}$	$\nu_{i,A}$ dimensionless	$q_{i,B,sat}$ mol/kg	$b_{i,B}$ $Pa^{-\nu_i}$	$\nu_{i,B}$ dimensionless
CO_2	1.5	2.85×10^{-15}	2.7	9.8	1.43×10^{-6}	1
CH_4	9.5	4.37×10^{-7}	1	3.7	6.7×10^{-9}	1
H_2	19	2.37×10^{-9}	0.87	20	1.61×10^{-8}	1
ethene	0.9	2.04×10^{-5}	1	4.9	6.97×10^{-9}	1.54
ethane	4.8	7.4×10^{-6}	1	1.3	2.89×10^{-10}	2
propene	1.5	2.45×10^{-10}	2.4	3.8	3.63×10^{-5}	1
propane	1.55	1.22×10^{-8}	2.13	3.3	7.57×10^{-5}	1

ZIF-8 CO_2/CH_4 unary and mixture permeances

Figure 28

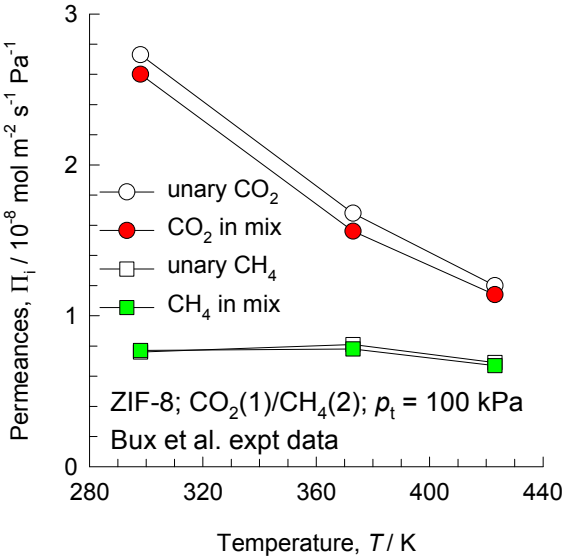

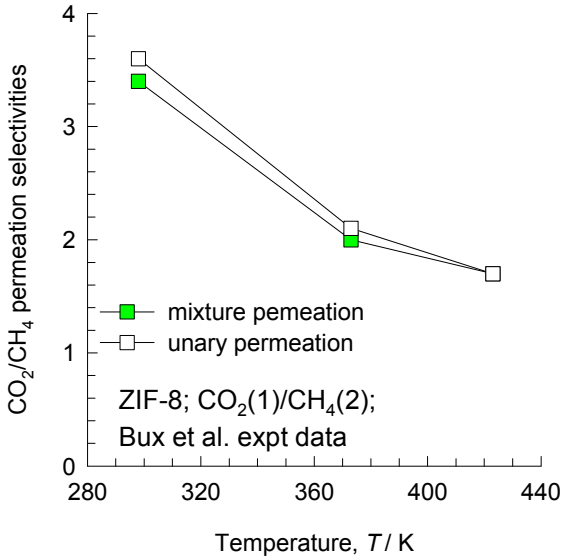

The data on membrane permeances are obtained from:

H. Bux, C. Chmelik, J.M. Van Baten, R. Krishna, J. Caro, Novel MOF-Membrane for Molecular Sieving Predicted by IR-Diffusion Studies and Molecular Modeling, Adv. Mater. 22 (2010) 4741-4743.

ZIF-8 ethane/ethane diffusion at 298 K: IRM experimental data

Figure 29

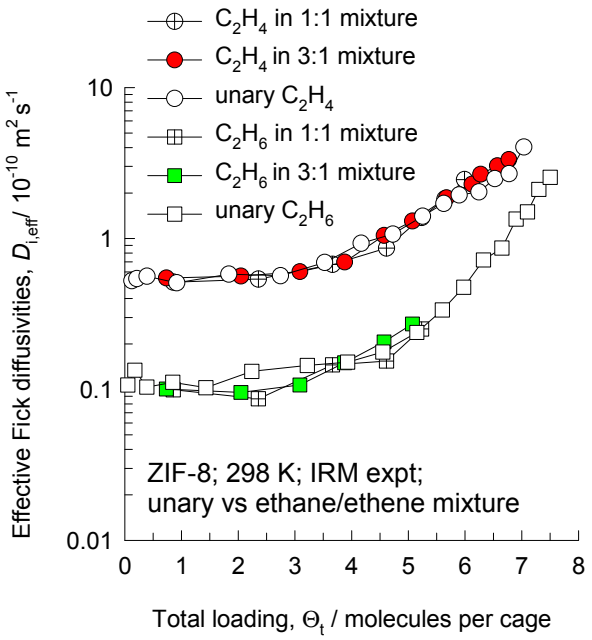

The IRM experimental data are re-plotted using the information in:

H. Bux, C. Chmelik, R. Krishna, J. Caro, Ethene/Ethane Separation by the MOF Membrane ZIF-8: Molecular Correlation of Permeation, Adsorption, Diffusion, J. Membr. Sci. 369 (2011) 284-289.

ZIF-8 ethene/ethane mixture permeances and transport coefficients

Figure 30

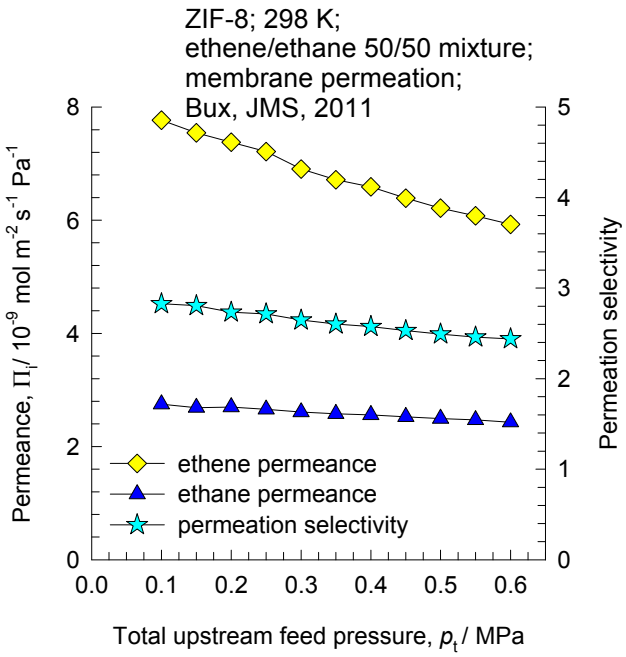

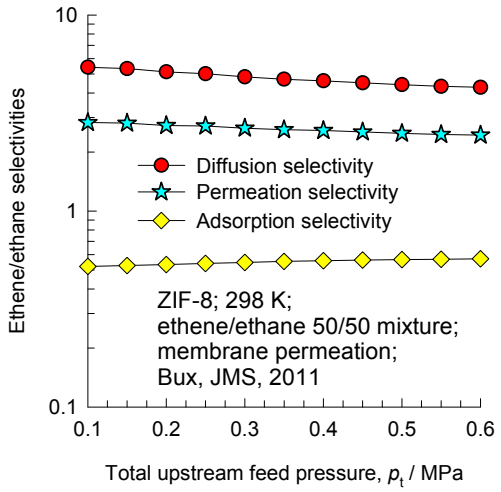

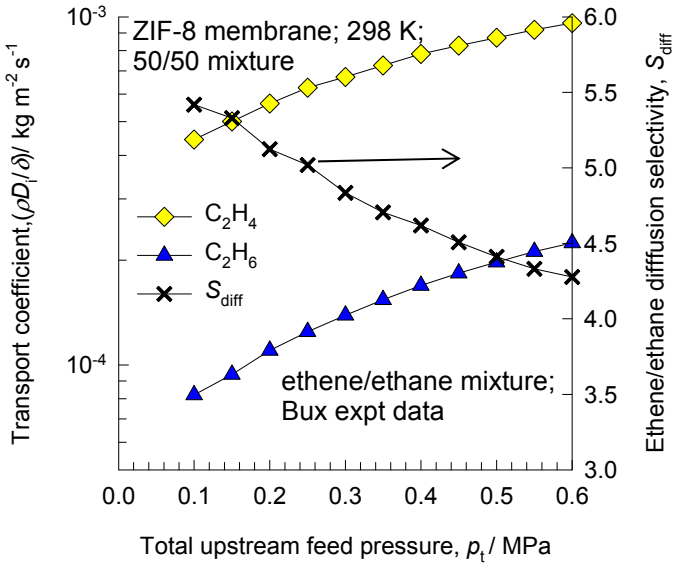

The data on membrane permeances are obtained from:

H. Bux, C. Chmelik, R. Krishna, J. Caro, Ethene/Ethane Separation by the MOF Membrane ZIF-8: Molecular Correlation of Permeation, Adsorption, Diffusion, J. Membr. Sci. 369 (2011) 284-289.

The calculations of S_{ads} are on the basis of IAST, with dual-Langmuir-Freundlich fits of pure component isotherms.

The transport coefficients are calculated from $$\frac{\rho D_i}{\delta} = \frac{\Pi_i}{\frac{q_i}{p_i}}$$

with the molar loadings q_i at the upstream face determined from IAST calculations.

ZIF-8 propene/propane mixture permeances and transport coefficients

Figure 31

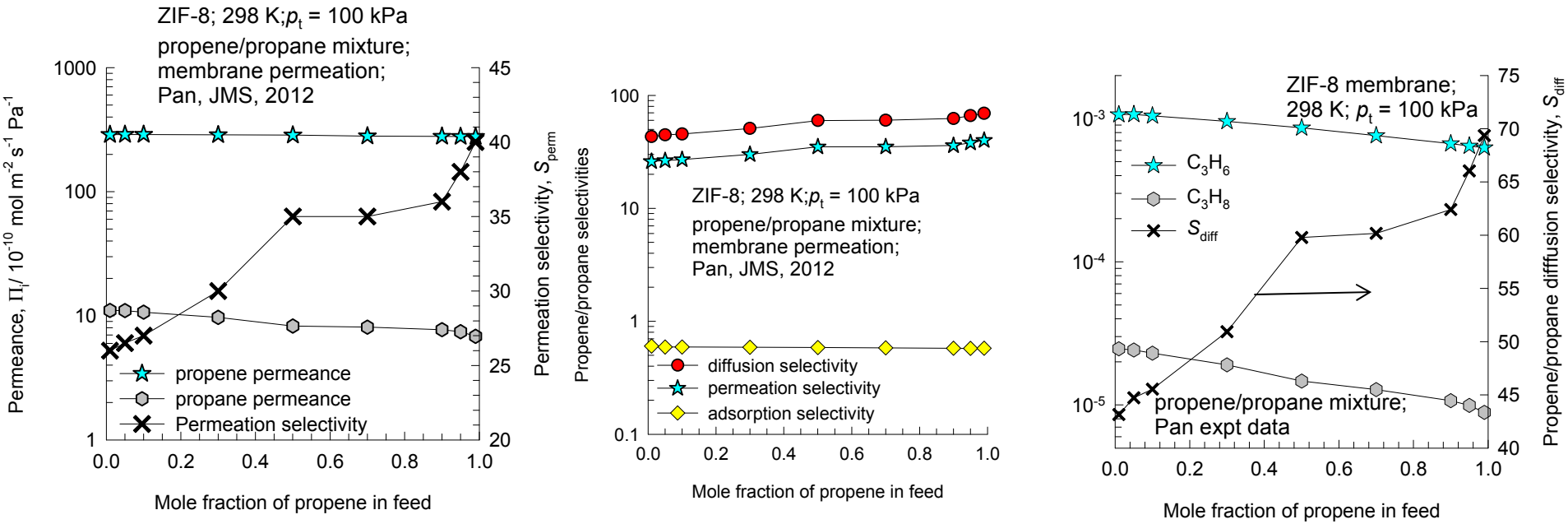

The data on membrane permeances are obtained from:

Y. Pan, T. Li, G. Lestari, Z. Lai, Effective Separation of Propylene/Propane Binary Mixtures by ZIF-8 Membranes, J. Membr. Sci. 390-391 (2012) 93-98.

The calculations of S_{ads} are on the basis of IAST, with dual-Langmuir-Freundlich fits of pure component isotherms.

The transport coefficients are calculated from $$\frac{\rho D_i}{\delta} = \frac{\Pi_i}{\frac{q_i}{p_i}}$$

with the molar loadings q_i at the upstream face determined from IAST calculations.

ZIF-8 propene/propane mixture permeances and transport coefficients

Figure 32

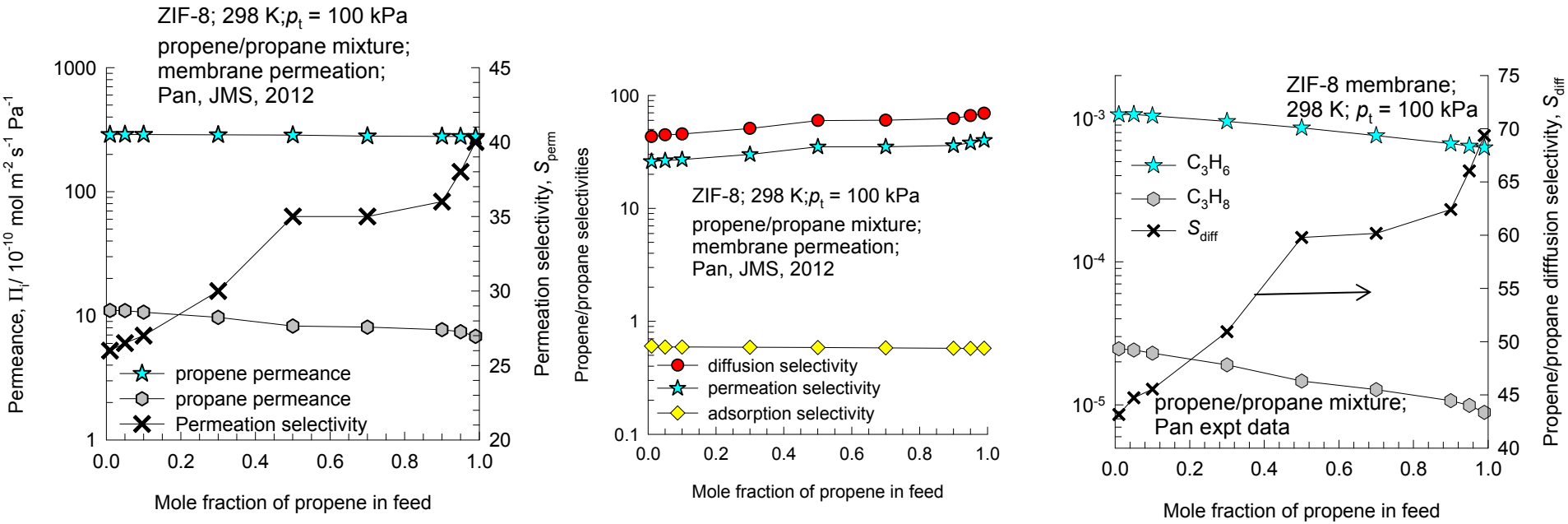

The data on membrane permeances are obtained from:

Y. Pan, T. Li, G. Lestari, Z. Lai, Effective Separation of Propylene/Propane Binary Mixtures by ZIF-8 Membranes, J. Membr. Sci. 390-391 (2012) 93-98.

The calculations of S_{ads} are on the basis of IAST, with dual-Langmuir-Freundlich fits of pure component isotherms.

The transport coefficients are calculated from $$\frac{\rho D_i}{\delta} = \frac{\Pi_i}{\frac{q_i}{p_i}}$$

with the molar loadings q_i at the upstream face determined from IAST calculations.

Figure 33

NiMOF-74

NiMOF-74 pore landscapes

Figure 34

The structural information on NiMOF-74 (= Ni_2(dobdc) = Ni\(dobdc = CPO-27-Ni) with dobdc = ($dobdc^{4-}$ = 2,5-dioxido-1,4-benzenedicarboxylatee)) were obtained from

A.Ö. Yazaydın, R.Q. Snurr, T.H. Park, K. Koh, J. Liu, M.D. LeVan, A.I. Benin, P. Jakubczak, M. Lanuza, D.B. Galloway, J.J. Low, R.R. Willis, Screening of Metal-Organic Frameworks for Carbon Dioxide Capture from Flue Gas using a Combined Experimental and Modeling Approach, J. Am. Chem. Soc. 131 (2009) 18198-18199.
D. Britt, H. Furukawa, B. Wang, T.G. Glover, O.M. Yaghi, Highly efficient separation of carbon dioxide by a metal-organic framework replete with open metal sites, Proc. Natl. Acad. Sci. U.S.A. 106 (2009) 20637-20640.
N.L. Rosi, J. Kim, M. Eddaoudi, B. Chen, M. O'Keeffe, O.M. Yaghi, Rod Packings and Metal-Organic Frameworks Constructed from Rod-Shaped Secondary Building Units, J. Am. Chem. Soc. 127 (2005) 1504-1518.
P.D.C. Dietzel, B. Panella, M. Hirscher, R. Blom, H. Fjellvåg, Hydrogen adsorption in a nickel based coordination polymer with open metal sites in the cylindrical cavities of the desolvated framework, Chem. Commun. (2006) 959-961.
P.D.C. Dietzel, V. Besikiotis, R. Blom, Application of metal–organic frameworks with coordinatively unsaturated metal sites in storage and separation of methane and carbon dioxide, J. Mater. Chem. 19 (2009) 7362-7370.
S.R. Caskey, A.G. Wong-Foy, A.J. Matzger, Dramatic Tuning of Carbon Dioxide Uptake via Metal Substitution in a Coordination Polymer with Cylindrical Pores, J. Am. Chem. Soc. 130 (2008) 10870-10871.

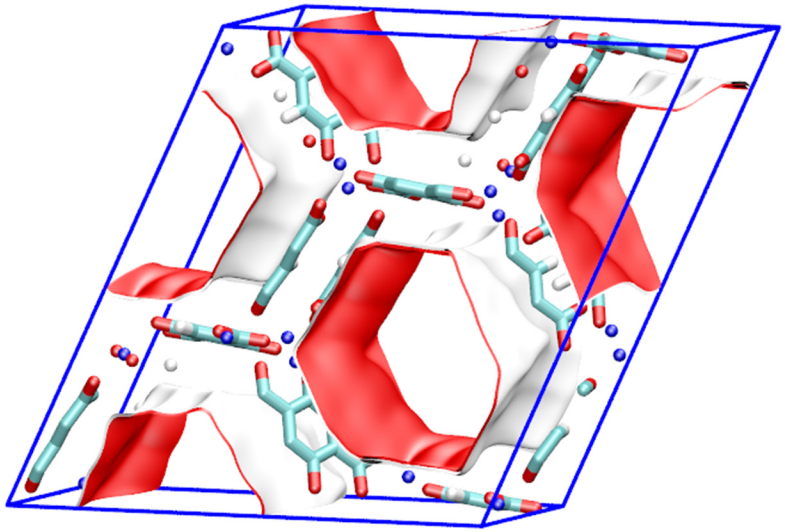

NiMOF-74 pore dimensions

Figure 35

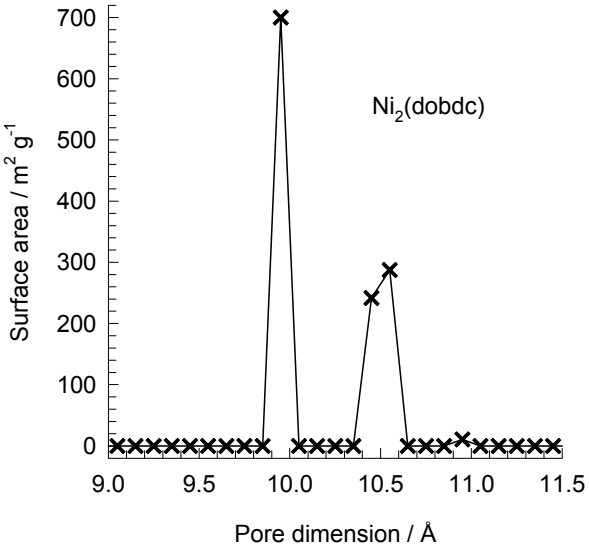

This plot of surface area versus pore dimension is determined using a combination of the DeLaunay triangulation method for pore dimension determination, and the procedure of Düren for determination of the surface area.

	NiMOF-74
a /Å	25.7856
b /Å	25.7856
c /Å	6.7701
Cell volume / Å^3	3898.344
conversion factor for [molec/uc] to [mol per kg Framework]	0.3568
conversion factor for [molec/uc] to [kmol/m^3]	0.6133
ρ [kg/m3]	1193.811
MW unit cell [g/mol(framework)]	2802.592
ϕ, fractional pore volume	0.695
open space / Å^3/uc	2707.6
Pore volume / cm^3/g	0.582
Surface area /m^2/g	1239.0
DeLaunay diameter /Å	9.80

NiMOF-74 fits of experimental isotherms for CO_2, CH_4, N_2, and H_2

Figure 36

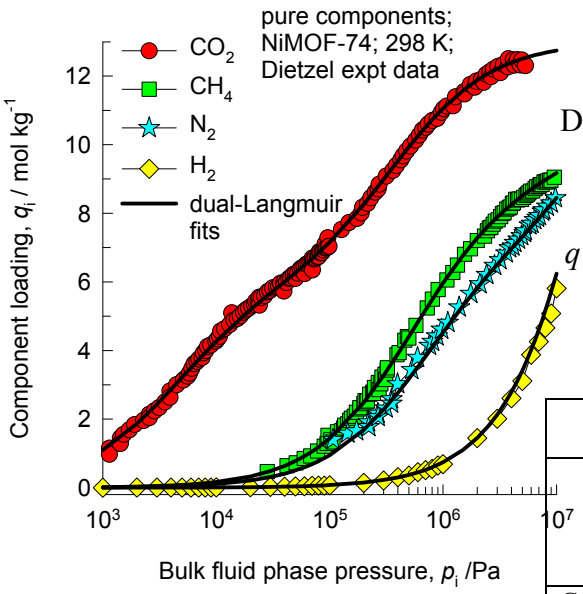

Dual-Langmuir-Freundlich parameter fits for NiMOF-74 (= Ni_2(dobdc) = CPO-27-Ni).

$$q = q_{A,sat}\frac{b_A p^{\nu_A}}{1+b_A p^{\nu_A}} + q_{B,sat}\frac{b_B p^{\nu_B}}{1+b_B p^{\nu_B}}; \quad b_A = b_{A0}\exp\left(\frac{E_A}{RT}\right); \quad b_B = b_{B0}\exp\left(\frac{E_B}{RT}\right)$$

	Site A				Site B			
	$q_{A,sat}$ mol kg^{-1}	b_{A0} Pa$^{-\nu_i}$	E_A kJ mol^{-1}	ν_A dimensionless	$q_{B,sat}$ mol kg^{-1}	b_{B0} Pa$^{-\nu_i}$	E_B kJ mol^{-1}	ν_B dimensionless
CO_2	7.1	1.22×10^{-10}	24.8	1	5.9	4.89×10^{-11}	38	1
CH_4	9	3.92×10^{-10}	21	1	2	9.52×10^{-12}	21	1
N_2	9.76	2.71×10^{-10}	10.6	1	7.35	6.57×10^{-10}	19.1	1
H_2	36	2.1×10^{-8}		1				

The isotherm fit parameters for CO_2, CH_4, and N_2 are on the basis of experimental data for variety of temperatures from:

P.D.C. Dietzel, V. Besikiotis, R. Blom, Application of metal–organic frameworks with coordinatively unsaturated metal sites in storage and separation of methane and carbon dioxide, J. Mater. Chem. 19 (2009) 7362-7370.

The isotherm fit parameters for H_2 are on the basis of experimental data from:
Yaghi, O. M. Hydrogen Storage in Metal Organic Frameworks, www.hydrogen.energy.gov/pdfs/review11/st049_yaghi_2011_p.pdf, University of California Los Angeles, California, 2011.

These H_2 isotherm data were supplemented with CBMC simulations.

NiMOF-74: Analysis of unary permeance data of Lee et al. (2012)

Figure 37

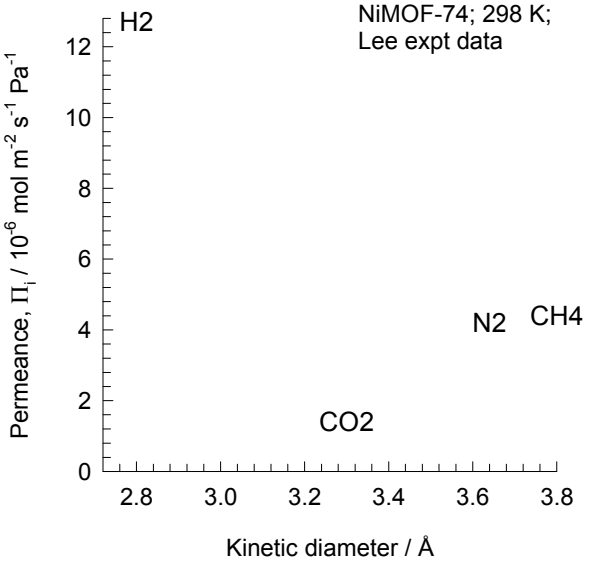

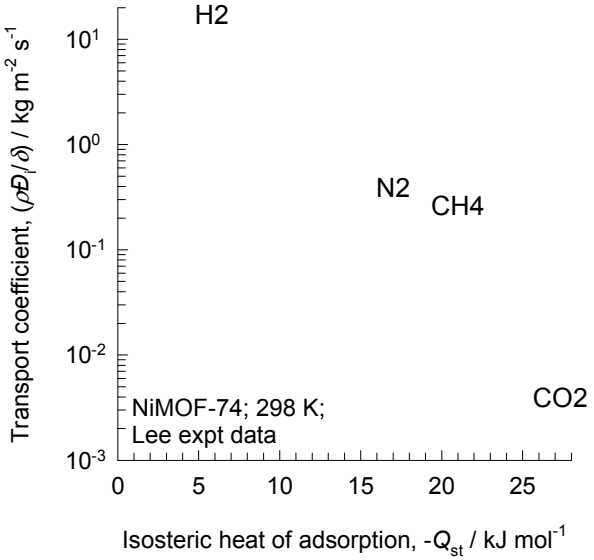

The data on membrane permeances are obtained from:

Lee, D. J.; Li, Q.; Kim, H.; Lee, K. Preparation of Ni-MOF-74 membrane for CO_2 separation by layer-by-layer seeding technique, *Microporous Mesoporous Mater.* **2012**, *163*, 169-177.

The transport coefficients are calculated from

$$\frac{\rho Đ_i}{\delta} = \frac{\Pi_i}{\Gamma_i \frac{q_i}{p_i}}$$

with the molar loadings q_i and thermodynamic correction factor Γ_i at the upstream face determined from pure component isotherm fits evaluated at p_i = 100 kPa

NiMOF-74: Maxwell-Stefan model calculations for H_2/CO_2 mixture permeation

Figure 38

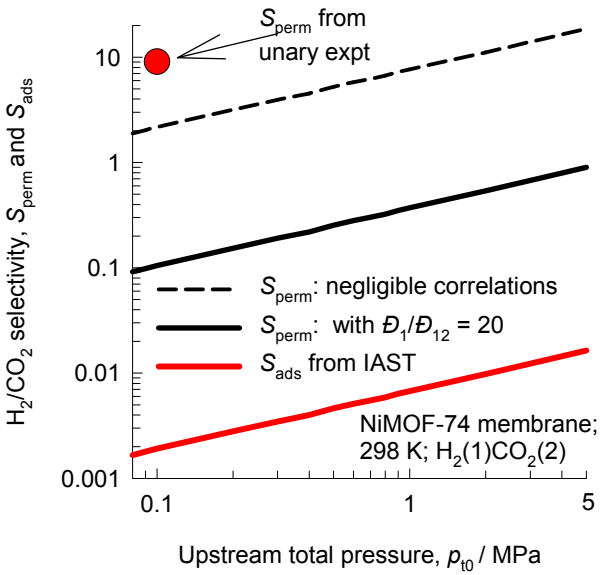

The inputs for the Maxwell-Stefan model are:

$$\frac{\rho Đ_1}{\delta} = 17 \ \text{kg m}^{-2} \ \text{s}^{-1}$$

$$\frac{\rho Đ_2}{\delta} = 0.015 \ \text{kg m}^{-2} \ \text{s}^{-1}$$

$$\frac{Đ_1}{Đ_{12}} = 20$$

$$\frac{Đ_2}{Đ_{12}} = 0.17647$$

NiMOF-74: Maxwell-Stefan model calculations for CH_4/CO_2 mixture permeation

Figure 39

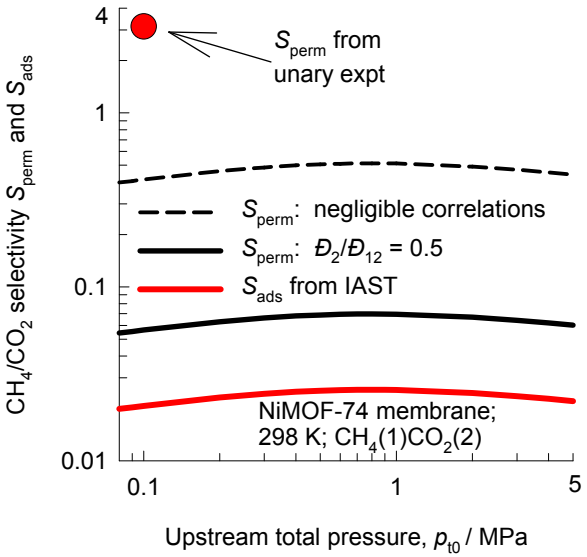

The inputs for the Maxwell-Stefan model are:

$$\frac{\rho Đ_1}{\delta} = 0.3 \ \text{kg m}^{-2} \ \text{s}^{-1}$$

$$\frac{\rho Đ_2}{\delta} = 0.015 \ \text{kg m}^{-2} \ \text{s}^{-1}$$

$$\frac{Đ_1}{Đ_{12}} = 10$$

$$\frac{Đ_2}{Đ_{12}} = 0.5$$

Figure 40

MFI

MFI pore landscape

	MFI
a /Å	20.022
b /Å	19.899
c /Å	13.383
Cell volume / Å^3	5332.025
conversion factor for [molec/uc] to [mol per kg Framework]	0.1734
conversion factor for [molec/uc] to [kmol/m^3]	1.0477
ρ [kg/m3]	1796.386
MW unit cell [g/mol(framework)]	5768.141
ϕ, fractional pore volume	0.297
open space / Å^3/uc	1584.9
Pore volume / cm^3/g	0.165
Surface area /m^2/g	487.0
DeLaunay diameter /Å	5.16

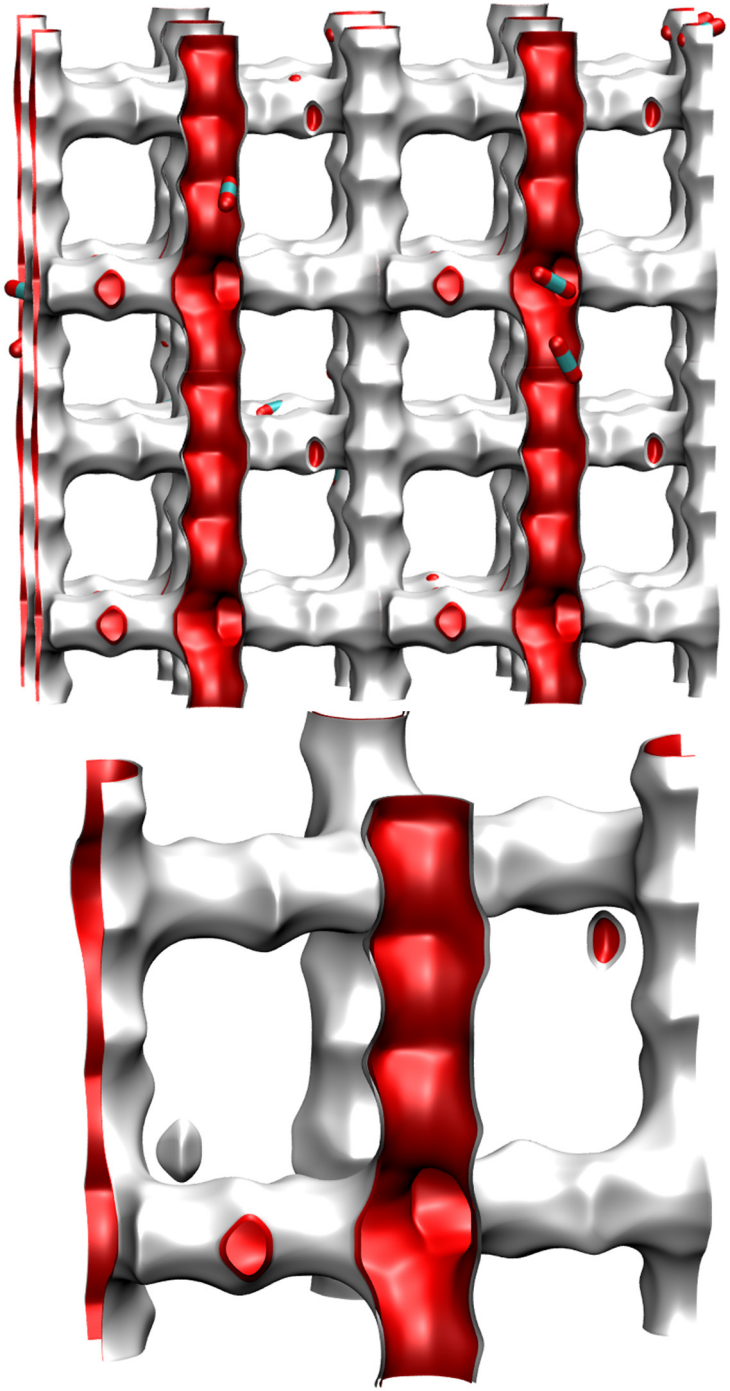

Structural information from: C. Baerlocher, L.B. McCusker, Database of Zeolite Structures, International Zeolite Association, http://www.iza-structure.org/databases/

MFI pore dimensions

10 ring channel of MFI viewed along [100]

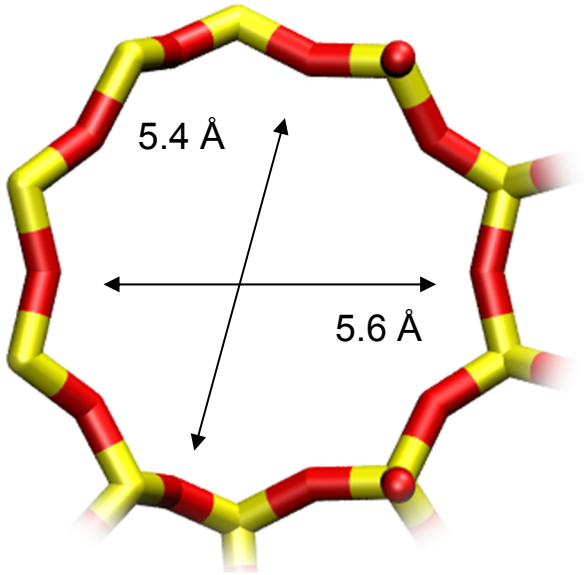

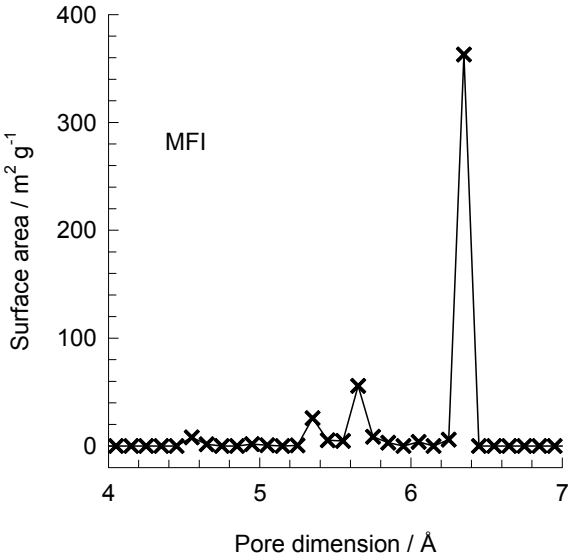

10 ring channel of MFI viewed along [010]

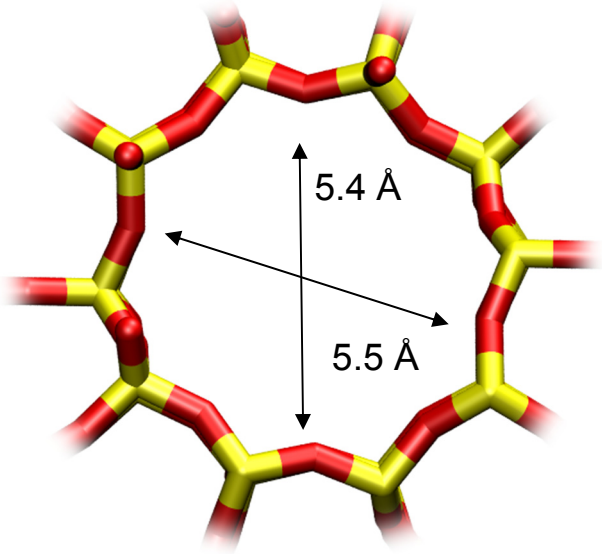

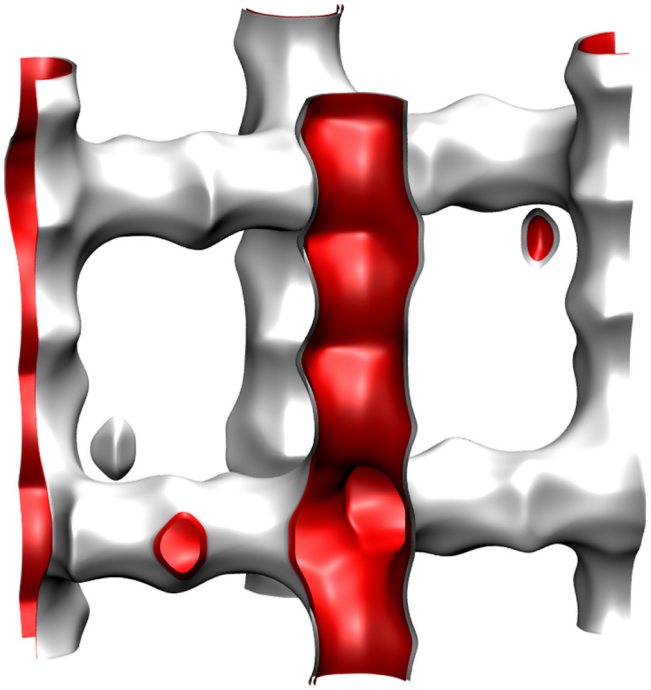

MFI pure component isotherm fits

Figure 43

Dual-site Langmuir-Freundlich parameters for pure component isotherms in MFI at 300 K. Note that the saturation capacities are specified in molecules per unit cell. Multiply these be 0.173366 to obtain the values in mol per kg framework. All the isotherm data are obtained by Configurational-Bias Monte Carlo (CBMC) simulations. These have been verified to be in good agreement with all available experimental isotherm data.

	Site A			Site B		
	$\Theta_{i,A,sat}$ molecules uc^{-1}	$b_{i,A}$ Pa$^{-\nu_i}$	$\nu_{i,A}$ dimensionless	$\Theta_{i,B,sat}$ molecules uc^{-}	$b_{i,B}$ Pa$^{-\nu_i}$	$\nu_{i,B}$ dimensionless
CO_2	19	6.12×10^{-6}	1	11	1.73×10^{-8}	1
CH_4	7	5×10^{-9}	1	16	3.1×10^{-6}	1
H_2	30	3.57×10^{-8}	1	42	1.39×10^{-9}	1
C_2H_6	3.3	4.08×10^{-7}	1	13	7.74×10^{-5}	1
C_3H_8	1.4	3.35×10^{-4}	0.67	10.7	6.34×10^{-4}	1.06
nC_4H_{10}	1.5	2.24×10^{-3}	0.57	8.7	9.75×10^{-3}	1.12

MFI: Snapshots of H_2/CO_2 mixture

Figure 44

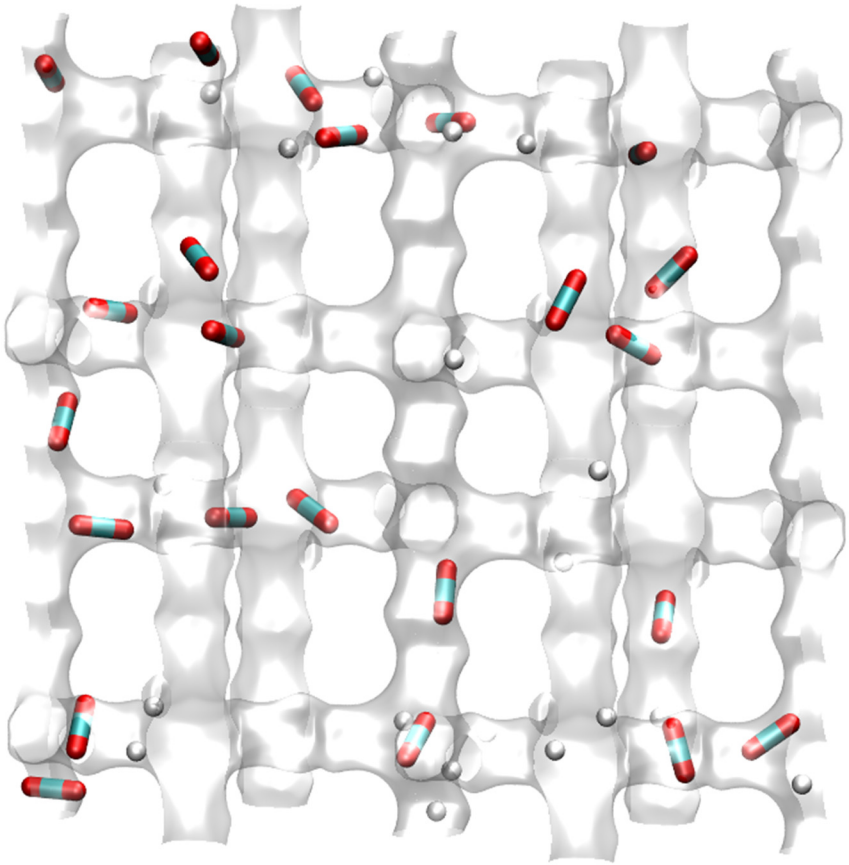

MFI: Maxwell-Stefan model calculations for H_2/CO_2 mixture permeation

Figure 45

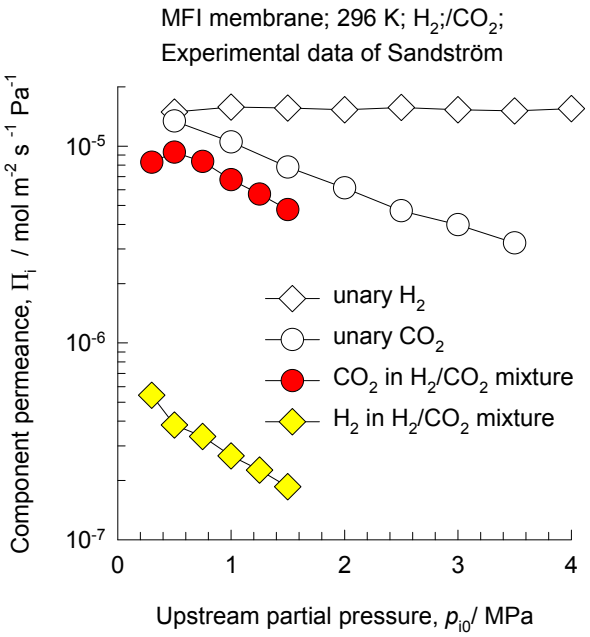

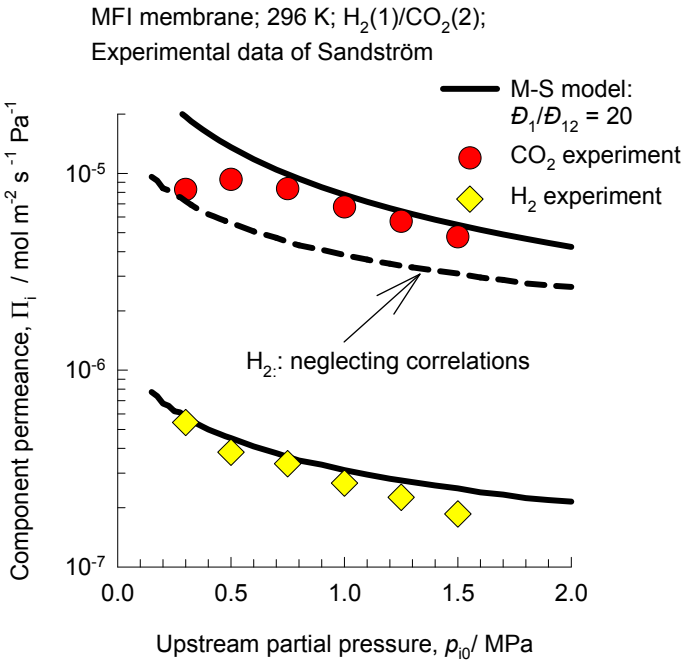

The experimental data are re-plotted using the information contained in:
L. Sandström, E. Sjöberg, J. Hedlund, Very high flux MFI membrane for CO_2 separation, J. Membr. Sci. 380 (2011) 232-240.

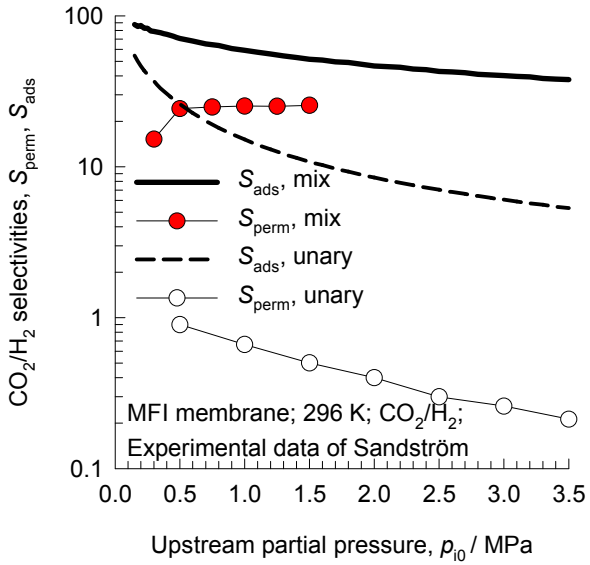

The inputs for the Maxwell-Stefan model are:

$$\frac{\rho Đ_1}{\delta} = 80 \ \text{kg m}^{-2} \ \text{s}^{-1}$$

$$\frac{\rho Đ_2}{\delta} = 2.7 \ \text{kg m}^{-2} \ \text{s}^{-1}$$

$$\frac{Đ_1}{Đ_{12}} = 20$$

$$\frac{Đ_2}{Đ_{12}} = 0.675$$

MFI: Maxwell-Stefan model calculations for CH_4/C_2H_6 mixture permeation

Figure 46

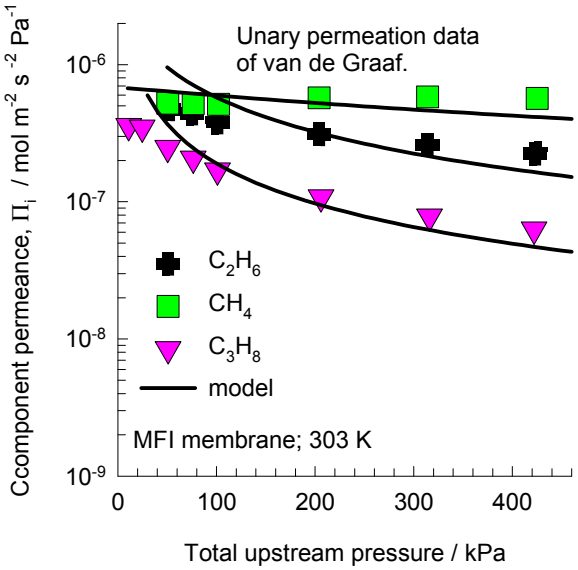

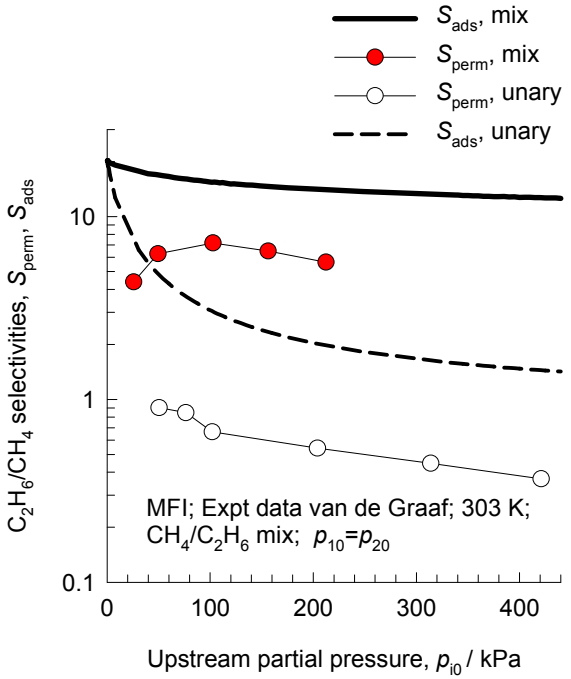

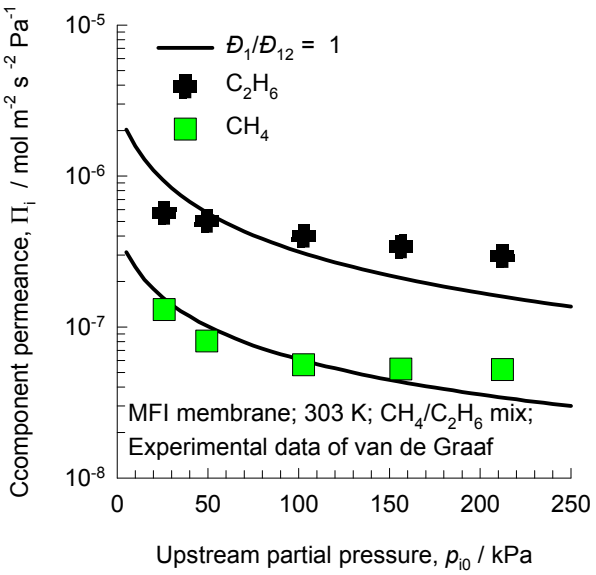

The experimental data are re-plotted using the information in: J.M. van de Graaf, F. Kapteijn, J.A. Moulijn, Modeling permeation of binary mixtures through zeolite membranes, A.I.Ch.E.J. 45 (1999) 497-511.

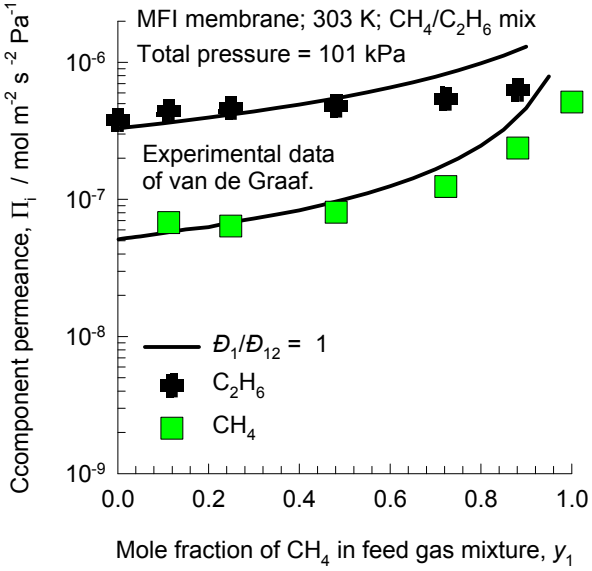

The inputs for the Maxwell-Stefan model are:

$$\frac{\rho Đ_1}{\delta} = 0.08 \ \text{kg m}^{-2} \ \text{s}^{-1}$$

$$\frac{\rho Đ_2}{\delta} = 0.016 \ \text{kg m}^{-2} \ \text{s}^{-1}$$

$$\frac{Đ_1}{Đ_{12}} = 1$$

$$\frac{Đ_2}{Đ_{12}} = 0.2$$

MFI: Maxwell-Stefan model calculations for CH_4/C_3H_8 mixture permeation

Figure 47

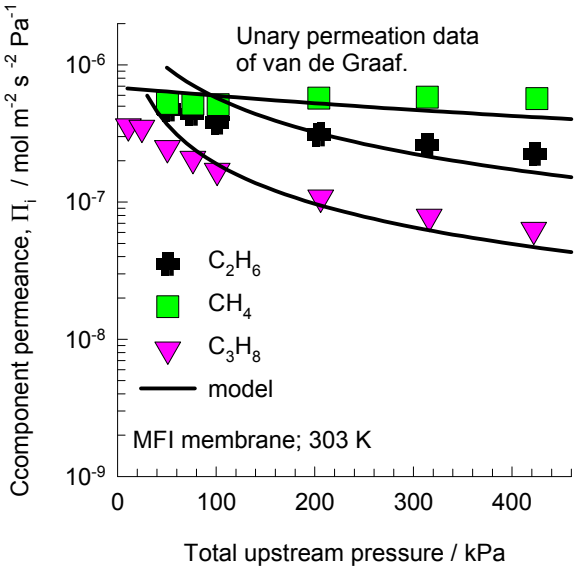

The experimental data are re-plotted using the information in: J.M. van de Graaf, F. Kapteijn, J.A. Moulijn, Modeling permeation of binary mixtures through zeolite membranes, A.I.Ch.E.J. 45 (1999) 497-511.

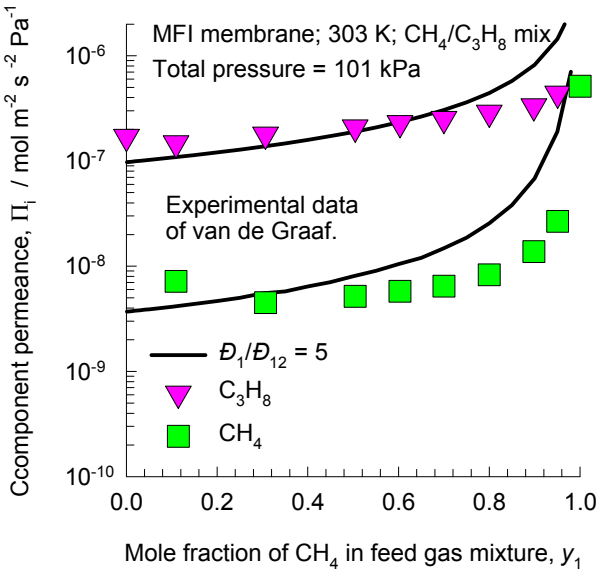

The inputs for the Maxwell-Stefan model are:

$$\frac{\rho Đ_1}{\delta} = 0.08 \ \text{kg m}^{-2} \ \text{s}^{-1}$$

$$\frac{\rho Đ_2}{\delta} = 0.005 \ \text{kg m}^{-2} \ \text{s}^{-1}$$

$$\frac{Đ_1}{Đ_{12}} = 5$$

$$\frac{Đ_2}{Đ_{12}} = 0.313$$

Figure 48

MFI: Maxwell-Stefan model calculations for transient CH_4/C_3H_8 mixture permeation

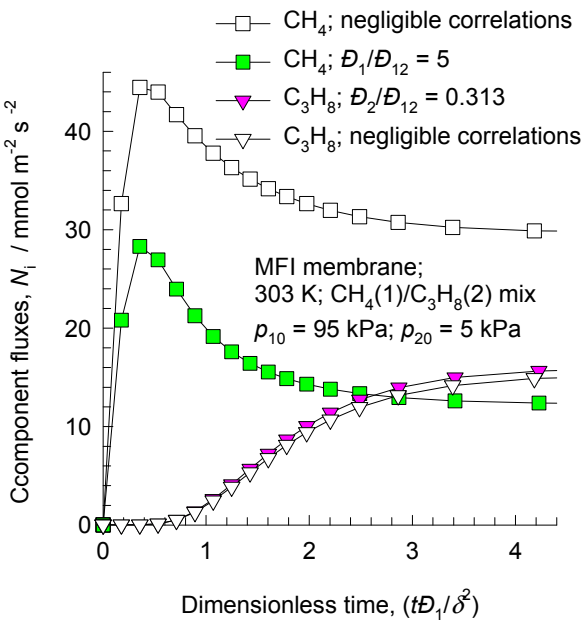

The inputs for the Maxwell-Stefan model are:

$$\frac{\rho Đ_1}{\delta} = 0.08 \ \text{kg m}^{-2} \ \text{s}^{-1}$$

$$\frac{\rho Đ_2}{\delta} = 0.005 \ \text{kg m}^{-2} \ \text{s}^{-1}$$

$$\frac{Đ_1}{Đ_{12}} = 5$$

$$\frac{Đ_2}{Đ_{12}} = 0.313$$

Figure 49

MFI: Maxwell-Stefan model calculations for CH_4/nC_4H_{10} mixture permeation

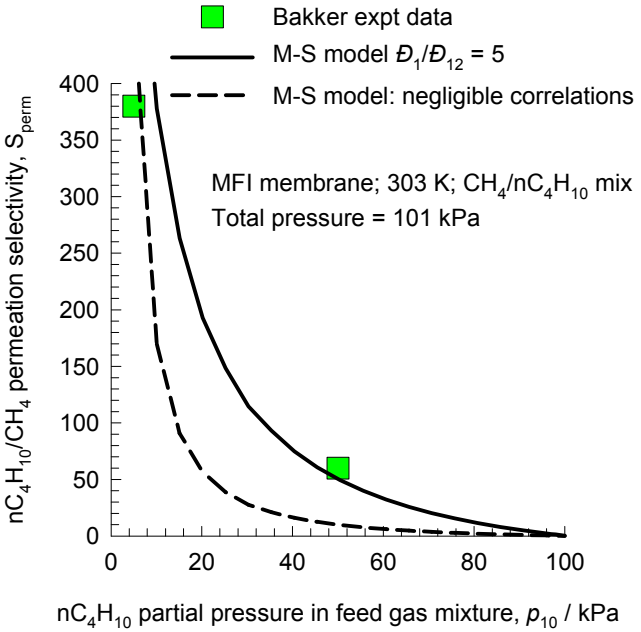

The experimental data are re-plotted using the information in:
W.J.W. Bakker, Structured systems in gas separation, Ph.D. Thesis, Delft University of Technology, Delft, 1999.

The inputs for the Maxwell-Stefan model are:

$$\frac{\rho Đ_1}{\delta} = 0.08 \ \text{kg m}^{-2} \ \text{s}^{-1}$$

$$\frac{\rho Đ_2}{\delta} = 0.003 \ \text{kg m}^{-2} \ \text{s}^{-1}$$

$$\frac{Đ_1}{Đ_{12}} = 5$$

$$\frac{Đ_2}{Đ_{12}} = 0.188$$

MFI CH_4/nC_4H_{10} mixture permeation fluxes, compared with unary fluxes

Figure 50

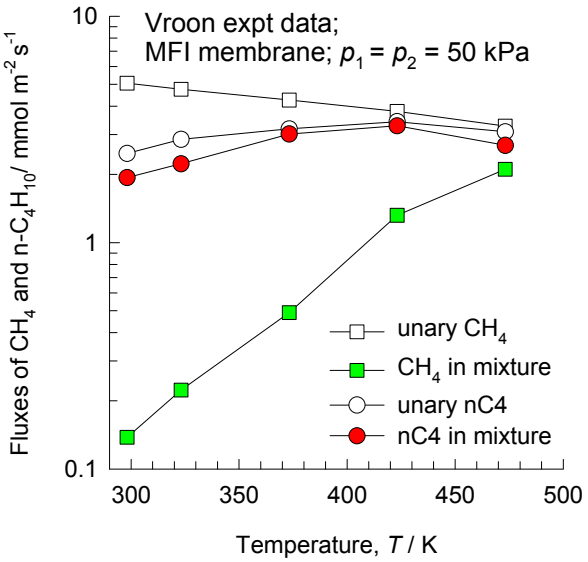

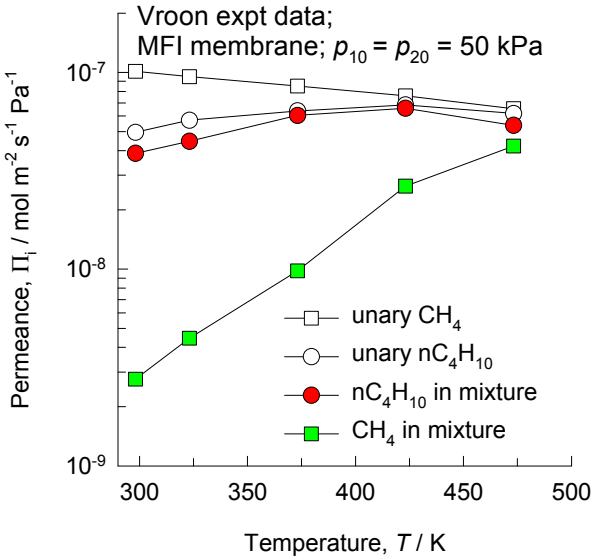

The experimental data are re-plotted using the information in:
Z.A.E.P. Vroon, K. Keizer, M.J. Gilde, H. Verweij, A.J. Burggraaf, Transport properties of alkanes through ceramic thin zeolife MFI membranes, J. Membr. Sci. 113 (1996) 293-300.

MFI nC_4H_{10}/H_2 transient mixture permeation

Figure 51

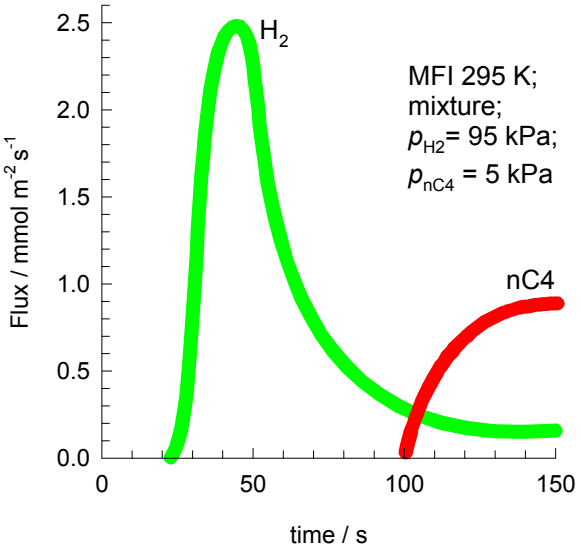

The experimental data are re-plotted using the information contained in:
W.J.W. Bakker, Structured systems in gas separation, Ph.D. Thesis, Delft University of Technology, Delft, 1999.

The theoretical analysis of this transient mixture permeation behavior is provided in our earlier works:
R. Krishna, R. Baur, Modelling issues in zeolite based separation processes, Sep. Purif. Technol. 33 (2003) 213-254.

MFI nC6/22DMB mixture permeation

Figure 52

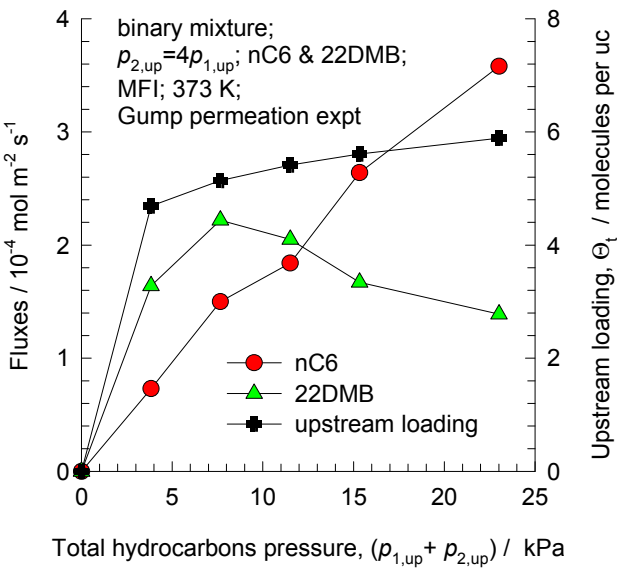

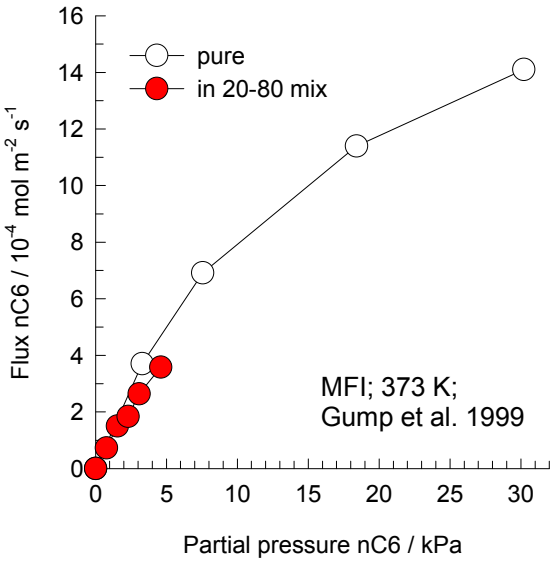

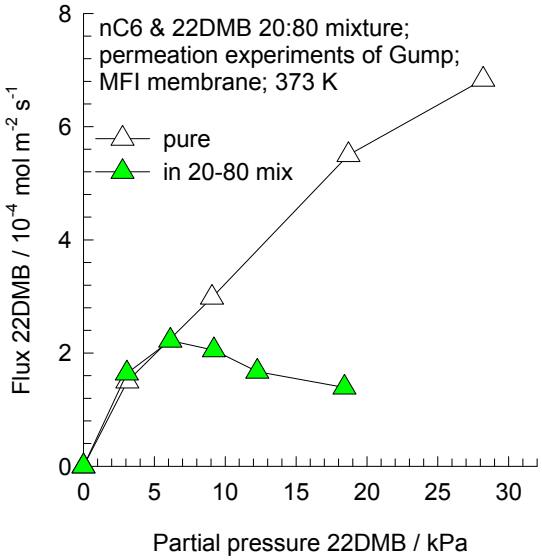

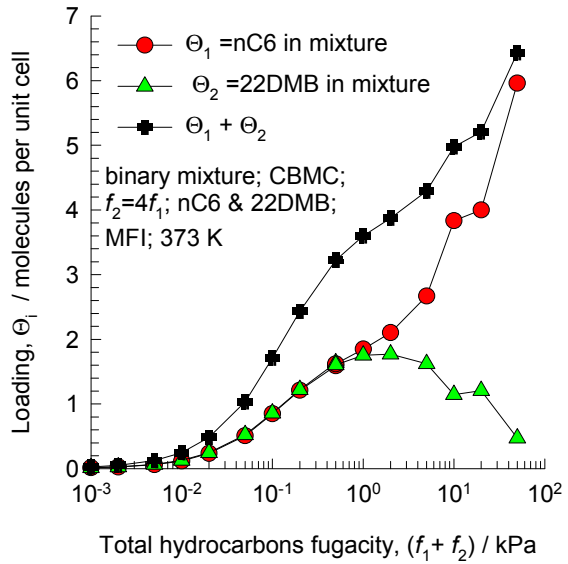

The experimental data are re-plotted using the information contained in:
C.J. Gump, R.D. Noble, J.L. Falconer, Separation of hexane isomers through nonzeolite pores in ZSM-5 zeolite membranes, Ind. Eng. Chem. Res. 38 (1999) 2775-2781.

The experimentally observed maximm in the flux of 22DMB is attributable to a corresponding maximum in the component loading as observed in CBMC simulations of mixture adsorption (shown on left). Further details of data interpretation is available in our previous works:
R. Krishna, J.M. van Baten, Screening of zeolite adsorbents for separation of hexane isomers: A molecular simulation study, Sep. Purif. Technol. 55 (2007) 246-255.
R. Krishna, Describing the diffusion of guest molecules inside porous structures, J. Phys. Chem. C 113 (2009) 19756-19781.

Figure 53

Snapshots showing the location of nC6/22DMB within MFI

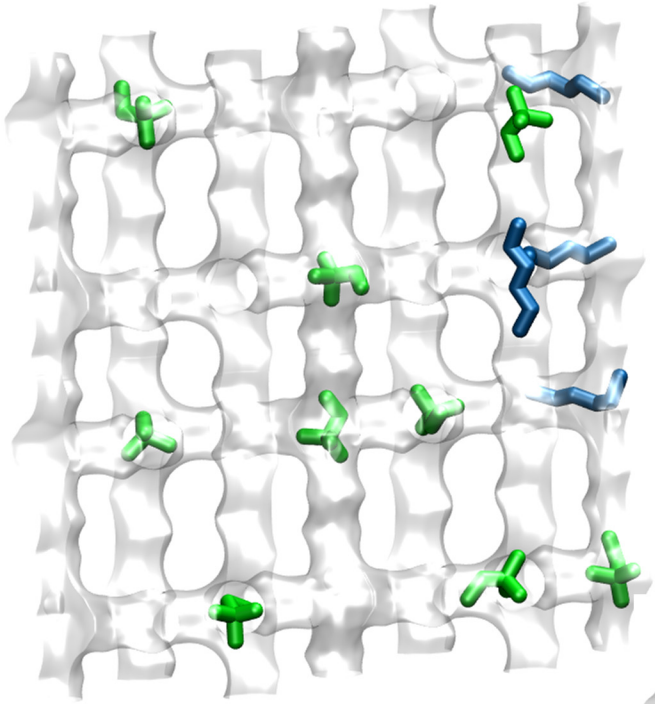

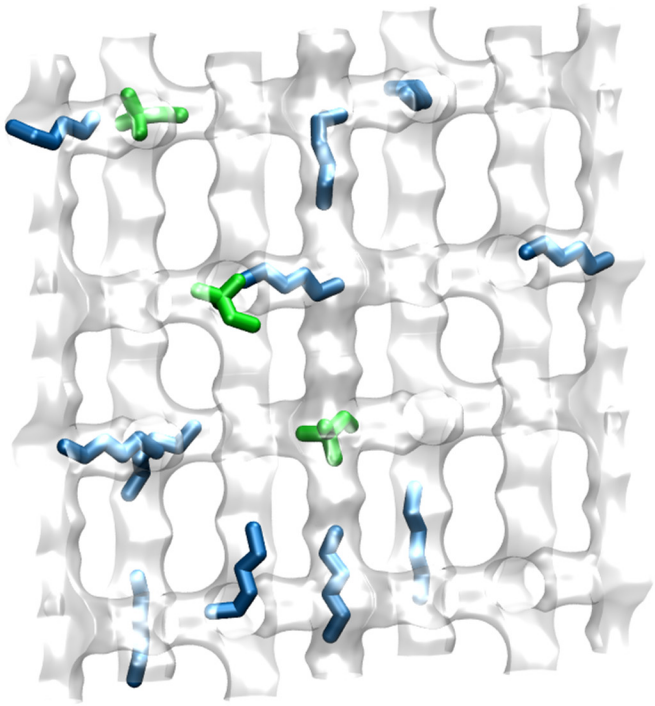

nC6 = 2 molecules/uc
22DMB = 2 molecules/uc